Journal of Structural Geology 31 (2009) 1556–1572

Contents lists available at ScienceDirect

Journal of Structural Geology

journal homepage: www.elsevier.com/locate/jsg

Understanding kinematic data from the Moine thrust zone in terms of a kinematics-based mathematical model of deforming thrust wedges

Matty Mookerjee [a,*,1], Gautam Mitra [b]

[a] Department of Geology, Sonoma State University, Rohnert Park, CA 94928, USA
[b] Department of Earth and Environmental Sciences, University of Rochester, Rochester, NY 14627, USA

ARTICLE INFO

Article history:
Received 25 January 2009
Received in revised form
20 August 2009
Accepted 21 August 2009
Available online 28 August 2009

Keywords:
Thrust sheet
Kinematics
Numerical model
Moine thrust
Shear zone
Strain

ABSTRACT

A salient–recess pair along the Moine thrust zone exhibits significant lateral, kinematic variations. Specifically, the more steeply dipping portion of the thrust surface, associated with the recess, shows evidence for greater strain magnitudes and more out-of-the-plane motion than the adjoining salient. Additionally, a subset of the grain-shape data has grain-shape approximations with their long axes oriented perpendicular to the regional transport direction. To more fully understand these kinematic features, we developed a kinematics-based mathematical model of thrust wedge deformation.

Our numerical model predicts an increase in strain magnitude as well as non-plane-strain flattening in the region of a thrust ramp, consistent with the strain patterns observed within the recess along the Moine thrust zone. Furthermore, in the absence of a lateral-confining boundary condition, much of the model thrust wedge experiences transport-perpendicular, maximum extension except for the region closest to the thrust where simple-shear deformation is dominant. Using our numerical model, we predict the amount of lateral-confining strain needed to induce plane-strain deformation (ε_{ps}) as well as the amount of lateral-confining strain necessary to make the long axis of the strain ellipsoid parallel with the transport direction ($\varepsilon_{parallel}$). We have found that the incremental $\varepsilon_{parallel}$ can be as much as 42% of the incremental strain magnitude. Thus, we consider transport-perpendicular lineations like those seen along the Moine thrust zone to be the result of lateral-confining boundary conditions that are weak enough to allow transport-perpendicular maximum extension.

1. Introduction

While modeling the kinematics of collisional tectonics, many investigators simply assume that deformation is plane strain and occurs along planar fault surfaces (e.g. Willet, 1992, 1999; Erickson and Jamison, 1995; Strayer and Hudleston, 1997, 1998; Smart et al., 1999). In detail, we know that these assumptions are inaccurate (e.g. Hossack, 1967; Durney and Ramsay, 1973; Mukul and Mitra, 1998; Twiss and Unruh, 1998; Kwon and Mitra, 2004; Strine and Mitra, 2004). Therefore, to advance numerical models further and to more fully understand kinematics in collisional environments, documenting non-plane-strain patterns, particularly in relation to non-planar thrust fault geometries, is important. The Moine thrust is a classic, well-exposed thrust zone that exhibits both non-plane strain and non-planar thrust fault geometries. The three-dimensional geometry of the thrust surfaces gives rise to salients (convex toward the foreland) and recesses (convex toward the hinterland) along the fault trace. Along the Moine thrust, between the localities of Loch More and the Stack of Glencoul, a salient–recess pair results from local fault steepening in the vicinity of the recess near Loch Srath nan Aisinnin (Fig. 1) (Butler, 1984). The comparison of kinematic data from the salient with similar data from the recess allows us to evaluate the effect of a non-planar fault geometry on fault zone kinematics.

To fully appreciate the field data from this salient–recess pair along the Moine thrust and the kinematic effects of the locally steepened fault surface, we developed a mathematical model for a deforming thrust wedge. Within our model, we input a flat–ramp–flat thrust geometry for our deforming wedge to simulate the effects of a locally steepened fault surface. While thrust wedge kinematics may be modeled in numerous ways (e.g. finite element modeling, finite difference modeling, distinct element modeling), we chose a purely kinematics-based approach that is controlled by assumptions about how various kinematic components vary throughout the wedge. These assumptions are based on generalizations made from field-based kinematic data. This approach precludes

* Corresponding author. Tel.: +1 707 664 2002; fax: +1 707 664 3975.
E-mail address: matty.mookerjee@sonoma.edu (M. Mookerjee).
[1] Formerly Matthew Strine.

0191-8141/$ – see front matter © 2009 Elsevier Ltd. All rights reserved.
doi:10.1016/j.jsg.2009.08.012

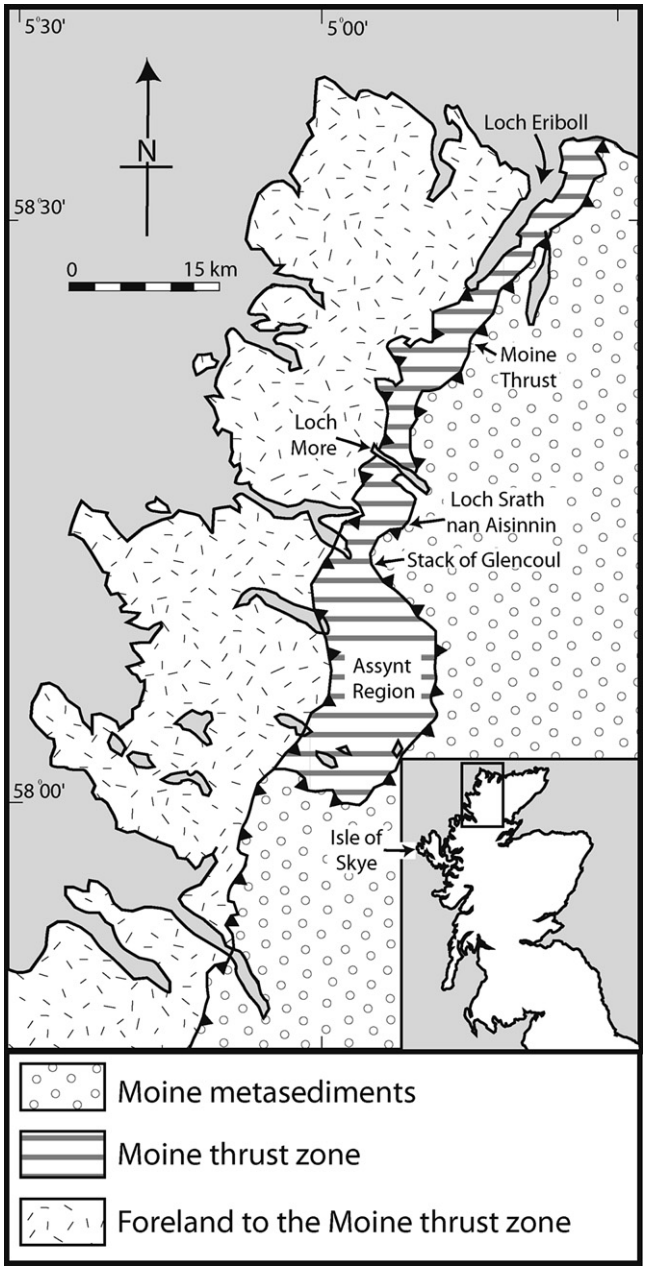

Fig. 1. Sketch map of Northern Scotland modified from Law et al. (1986) showing the location of the Moine thrust zone and the trace of the Moine thrust.

assumptions about tectonic stresses and associated boundary conditions that are required for mechanics-based models. Additionally, we do not assume a flow law for the deforming material, which is likely to vary with depth as well as time (Gilotti and Kumpulainen, 1986; Wojtal and Mitra, 1986, 1988; Gilotti, 1992).

Our general approach for this numerical model is to use a series of lines of observation points that are initially fault perpendicular, which are tracked as they move either through (hanging wall) or beneath (footwall) the deforming wedge. With each increment of deformation, an individual observation point experiences a component of pure strain and, within the hanging wall, translation parallel to the dip of the fault. The pure strain deformation is comprised of five strain components: 1) thrust-parallel simple shear, 2) thrust-normal reaction strain, 3) horizontal contraction strain, 4) vertical gravitational strain, and 5) a lateral-confining strain. We use a series of assumptions to describe the variation of the strain components within and underneath the wedge. In this way, a deformation matrix is assembled for each observation point at each incremental position. The deformation matrices are used to determine both the strain path and the particle path for each of the observation points.

2. Geological setting

2.1. The Moine thrust zone

The Moine thrust zone is a series of NNE–SSW trending, ESE dipping ductile deformation zones that cross the NW Highlands of Scotland (Fig. 1). This thrust zone formed during the Caledonian orogeny when the continents of Baltica and Laurentia collided in the Early Silurian (Cocks and Torsvik, 2006). Prior to this collision, Northern Scotland was part of the continental margin of Laurentia where Proterozoic through Ordovician sediments accumulated (e.g. Cambrian Eriboll Sandstone and Cambrian–Ordovician Durness Limestone) (Peach et al., 1907). During the Caledonian orogeny, these units became part of the foreland fold–thrust belt of the Moine thrust zone.

The Moine thrust zone is a classic and well-exposed example of a fold–thrust belt. The chronology of thrusting generally represents a typical break-forward sequence of which the Moine thrust is the easternmost and oldest within the zone (Peach et al., 1907; Elliott and Johnson, 1980; Coward, 1988; Holdsworth et al., 2006). Regional isograds seen in the calc-silicate Moine metasediments are parallel to the thrusts and decrease in grade in the direction of thrusting (Johnson, 1983). In general, the tectonic foliation within individual thrust sheets is sub-parallel to the associated thrust surface and the penetrative lineation is approximately parallel to the down-dip direction of the fault. Fault rocks within the Moine thrust zone are often folded with wavelength and amplitude increasing away from the thrust surface. Sheath folds are common (Carreras et al., 1977; Evans and White, 1984; Holdsworth, 1990; Alsop and Holdsworth, 1999; Strine and Wojtal, 2005).

The Moine thrust itself spans ≈190 km from the northern coast of Scotland (at Whiten Head) to the Isle of Skye on the west coast (Fig. 1). The Moine thrust was active as a ductile deformation zone from 443–435 Ma to 430 Ma (van Breemen et al., 1979; Johnson et al., 1985; Kelley, 1988; Freeman et al., 1998; Dallmeyer et al., 2001). It carries Proterozoic Moine metasediments over late Proterozoic to Ordovician sedimentary rocks and Archean basement rocks. The regional transport direction was 290–295° as defined by the penetrative lineations within fault rocks (Cloos, 1946; Coward et al., 1992). Adjacent to the thrust surface, mylonite zone thickness varies from 0 to 250 m (Peach et al., 1907; Christie, 1960, 1963; Evans and White, 1984; Highton et al., 2002). These fault rocks were retrograde metamorphosed to lower greenschist facies (Kelley and Powell, 1985; Johnson et al., 1985; Harris and Johnson, 1991; Freeman et al., 1998). Elliott and Johnson (1980) determined a minimum thrust displacement of 75 km based on balanced cross-sections.

2.2. The Moine thrust between Loch More and the Stack of Glencoul

Near the center of the trace of the Moine thrust is a large recess known as the Assynt Culmination where the thrust surface rises to an elevation of 1 km greater than the surrounding thrust surface (Elliott and Johnson, 1980). The Assynt Culmination formed when the thrust surface was folded into a doubly plunging anticline by the emplacement of a series of footwall imbricates. To the NNE of the Assynt Culmination is a smaller recess that formed in a similar

fashion between the Stack of Glencoul and Loch More (Butler, 1984) (Fig. 1). In this area, the Moine thrust places Proterozoic Moine schists onto Cambrian quartzites (i.e., the Pipe Rock and Basal Quartzite units). Within this recess, near Loch Srath nan Aisinnin, the mylonite layer is about 70 m thick and thins toward the adjoining salient to the south. The footwall rocks closest to the Moine thrust are extensively recrystallized, while, farther from the thrust, relict detrital grains are distinguishable. Additionally, at the Stack of Glencoul and nowhere else in our field area, there is evidence of a later brittle deformation, the exact nature of which is still debated (e.g. Holdsworth et al., 2006). We suggest that this later motion, whether normal or reverse, is likely to be relatively minor (10s to 100s m) and does not cause significant problems in deciphering the earlier plastic history.

3. Methods

3.1. Quartz c-axis measurements

We collected ninety quartzite samples from the footwall around the salient–recess pair (Figs. 2 and 3). From each sample, three mutually perpendicular thin-sections were cut: perpendicular to the lineation and normal to the foliation; parallel to the lineation and normal to the foliation; parallel to the foliation. Quartz *c*-axis orientations were measured optically using a petrographic microscope and universal stage. We made no fewer than one hundred *c*-axis measurements per section (i.e. a minimum of 300 measurements per sample) and then rotated those data into a common reference frame, the lineation-parallel, foliation-normal

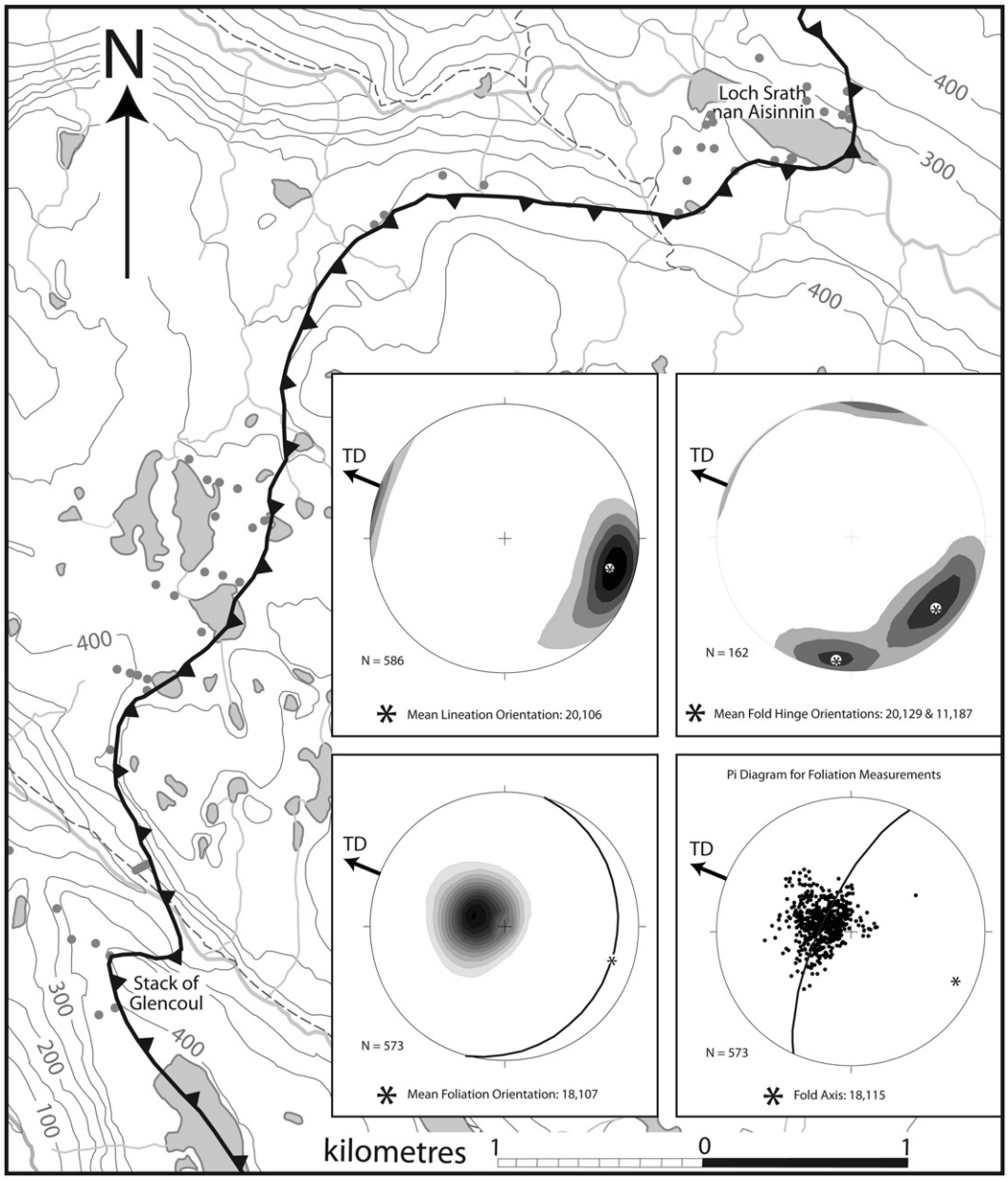

Fig. 2. Generalized topographic map of salient near the Stack of Glencoul with macroscopic field data collected from this area. Topographic contours are given in meters. The dots represent sampling localities. The data is plotted on lower hemisphere equal-area projections with 5% contour intervals. TD is the regional transport direction, 292.5°. Dashed lines are trails, light gray lines are streams, and gray areas are lochs.

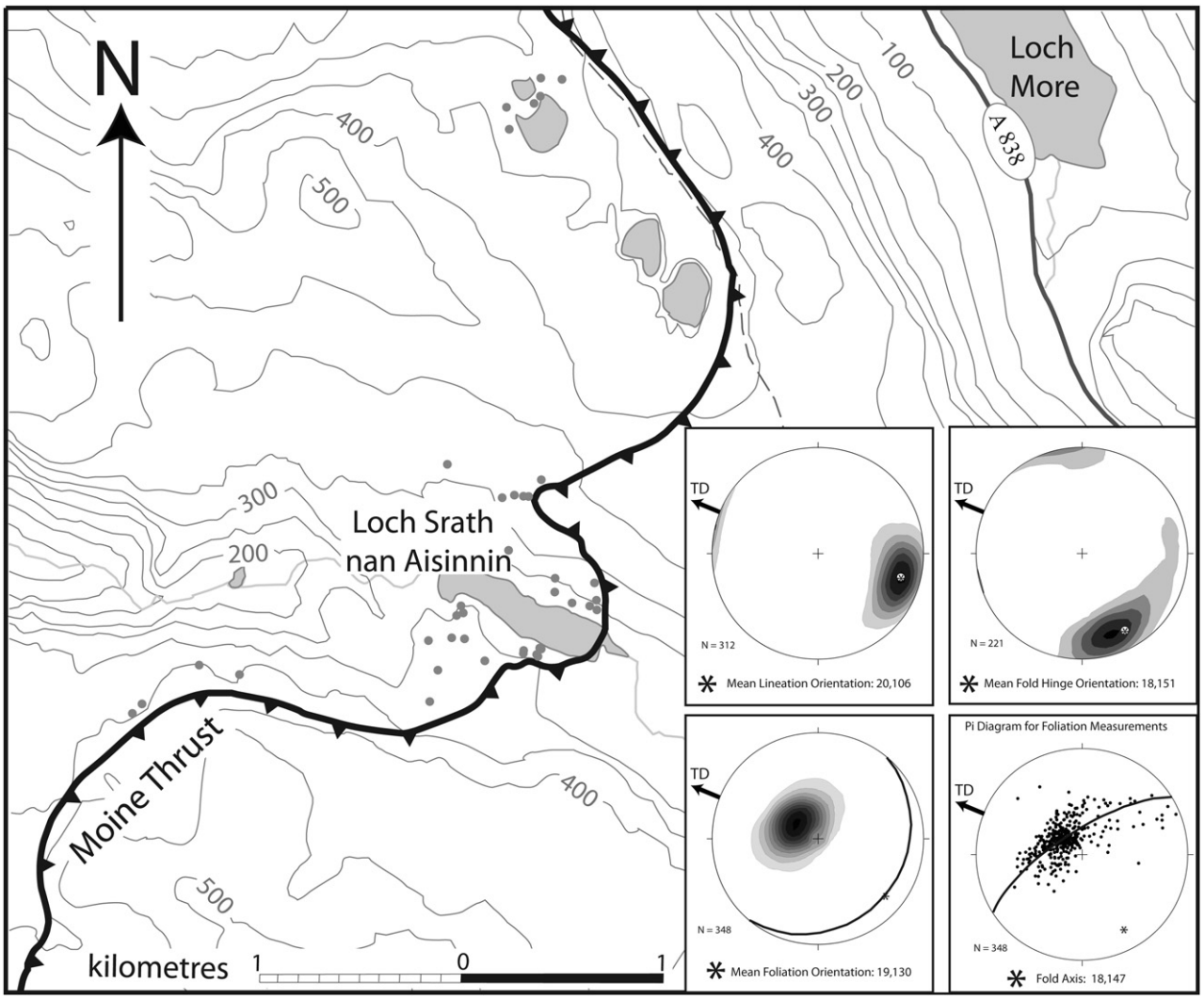

Fig. 3. Generalized topographic map of the recess near Loch Srath nan Aisinnin with macroscopic field data collected from this area. Topographic contours are given in meters. The dots represent sampling localities. The data is plotted on lower hemisphere equal-area projections with 5% contour intervals. TD is the regional transport direction, 292.5°. Dashed lines are trails, light gray lines are streams, and gray areas are lochs.

plane. These data were then plotted on lower hemisphere, equal-area projections such that the foliation is vertical and striking "left–right" and the lineation is horizontal. For the sake of consistency, we only measured *c*-axis from relict detrital grains in samples that have these grains available. For eight samples within the recess, our optically measured patterns were verified by Holger Stunitz at the University of Basel, Switzerland, using X-ray goniometry.

3.2. Three-dimensional grain-shape data

Most of the elliptical grain-shape approximations were determined in part by using NIH Image (v. 1.62). For each thin-section, between 3 and 10 fields of view were digitally captured and printed using Spot Advanced (v. 3.5.9 for Windows). With the use of a light-table, we traced the outline of individual grains onto an overlay. We then scanned these overlays and modified the files using Adobe Photoshop (filled in the inter-grain space, inverted the image and cropped). These images were then imported into NIH Image, which determines the elliptical best-fit for each of the outlined grain sections and then outputs the major and minor axis lengths and the angle between the long axis and the horizontal axis, θ'. For eleven of the ninety samples measured for grain-shape approximations, we measured the long and short axis lengths directly from the microscope using the graduated cross-hairs and measured the angular orientation, θ', via stage rotation. For both methods, θ' is measured from the lineation for the lineation-parallel, foliation-normal plane and the foliation-parallel plane, and from the foliation plane in the lineation-perpendicular, foliation-normal plane. Borradaile (1984) showed that a sample size of more than 50–75 elliptical markers ceased to refine the grain-shape estimation; thus, we felt comfortable with measuring approximately 100 grains per section.

Next, we imported these data into a Mathematica (v. 4.1) notebook, which combines the data for each section and calculates the vector and harmonic means as defined by Lisle (1985) for each of the three sections for a given sample. It is important to note that the vector mean formula assumes that the long axis of each grain will be $\pm 45^\circ$ from the reference line (0°). Since this geometry is not always the case, we rotated our data such that they are approximately centered about the reference line, determined the vector mean, and then subtracted the amount of rotation from the vector mean.

Using the vector and harmonic mean for each section, our Mathematica notebook calculates the best-fit ellipsoidal grain-shape approximation. The best-fit method, outlined in Strine and Wojtal (2004), takes a least squared approach. From the resulting

best-fit ellipsoid, axes lengths and associated strains were calculated along with Flinn's (1962) *k*-value, Lode's ratio (ν) (Hossack, 1967), and octahedral shear strain (ε_s) (Nadai, 1963). The best-fit ellipsoids were rotated from the kinematic reference frame into the geographic reference frame, and the orientation of each of the ellipsoid axes were calculated.

Orientation data were plotted and contoured using either Johannes Duyster's StereoNett (v. 2.46), or Haneberg's Mathematica package (2004). Richard Allmendinger's StereoNet program was used to calculate best-fit great circles. Mean orientations were calculated in Mathematica (v. 4.1).

4. Field data

4.1. Macroscopic fabric measurements

Within the salient, we collected lineation, foliation and fold hinge orientations from the footwall and hanging wall rocks (Fig. 2). The mean lineation orientation, 20°, 106°, and the down-dip direction of the mean foliation orientation, 18°, 107°, are sub-parallel to the regional transport direction (i.e. 290–295°). Additionally, we observed a modest number of weak stretching lineations oriented subperpendicular to the transport direction. The mean fold hinge measurements have a bimodal distribution with one mean nearly parallel to the transport direction and the other nearly perpendicular to the transport direction. This distribution of fold hinge orientations supports the observation that both sheath folds and cylindrical folds exist within this area (Strine and Wojtal, 2005). We constructed a π-diagram and determined a fold axis of 18°, 115° which is, again, sub-parallel to the transport direction and consistent with the observed sheath folds (Fig. 2).

Within the recess near Loch Srath nan Aisinnin, similar macroscopic measurements were taken from the deformed footwall and hanging wall rocks (Fig. 3). The mean lineation orientation, 20°, 106°, is sub-parallel to the regional transport direction, as is the down-dip direction of the mean foliation orientation, 19°, 130°. However, the mean hinge line orientation, 18°, 151°, is oblique to the transport direction (Fig. 3). The fold axis orientation, 18°, 147°, which was determined using a π-diagram, is sub-parallel to the mean hinge orientation and therefore is also oblique to the regional transport direction. While the origin of the obliquity of these folds remains unclear (see discussions in Strine and Wojtal, 2004, 2005; Alsop and Holdsworth, 2005), these folds do post-date the formation of the penetrative foliation and lineation.

4.2. Microstructures

The footwall quartzites display a variety of microstructures along strike in the salient–recess pair. In the salient, the quartzites exhibit a shape preferred orientation, indented grain contacts, undulose extinction, minor quartz overgrowths, and some evidence for low-temperature grain-boundary migration (i.e. bulging recrystallization) (Fig. 4a). At the Stack of Glencoul (Fig. 2) where the thrust contact is excellently exposed, the rocks display Regime

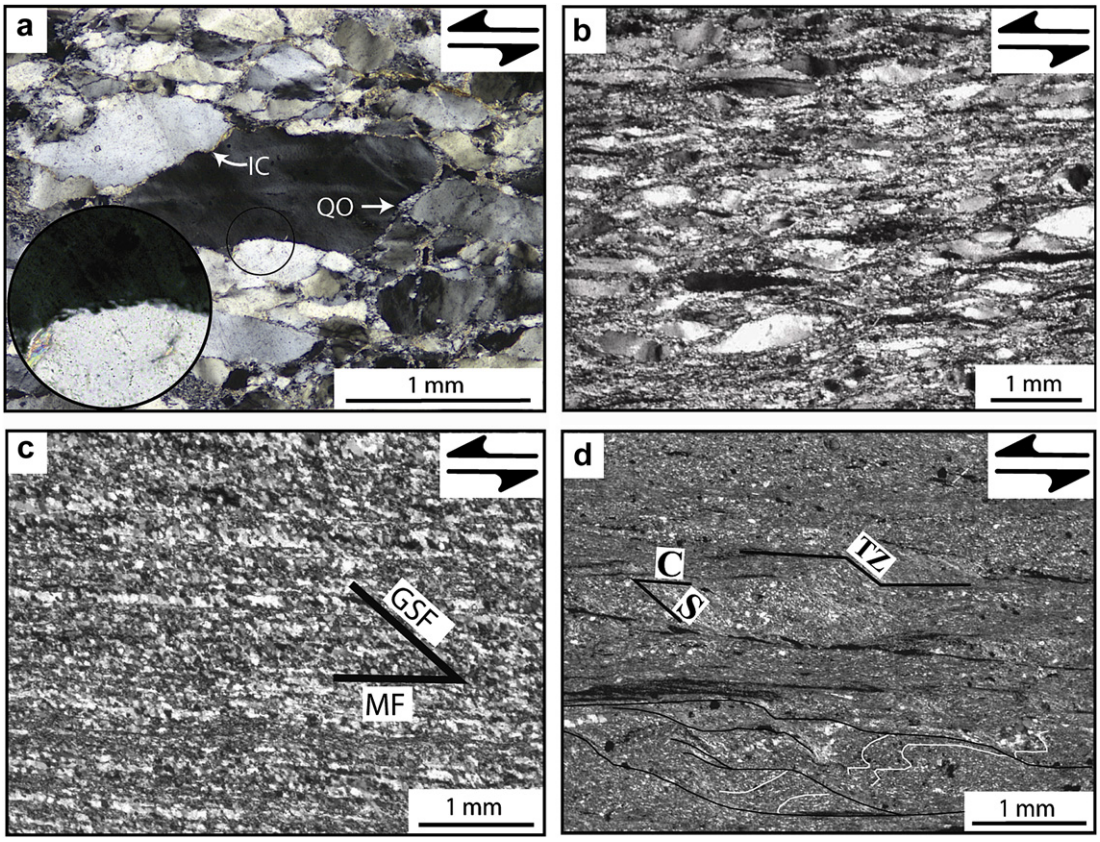

Fig. 4. Crossed nicols photomicrographs of fault rocks from the salient–recess pair. All photomicrographs are taken from the lineation-parallel, foliation-normal plane with the bottom of the photographs parallel to the lineation-direction and looking NNE. a) Deformed quartz grains from the footwall of the salient showing undulose extinction, sub-horizontal deformation bands, indented grain contacts (labeled IC), quartz overgrowths (labeled QO), and bulging grain boundaries (in circular blow-up), b) deformed relict grains from the footwall of the recess, c) recrystallized footwall quartzite from the recess. MF is the mylonitic foliation and GSF is the recyrstallized grain-shape foliation, d) hanging wall Moine Schist from the recess. S-C fabric defined by thin phyllosilicate layers where (S) oriented obliquely to the mylonitic banding (C), which is defined by nearly continuous and planar phyllosilicate layers extending across the field of view. Near the center of the field of view there is a "transfer zone" within the phyllosilicate-rich layer (TZ). White lines delineate some intrafolial folds.

II type microstructures (Hirth and Tullis, 1992). Subgrains and new grains have formed via subgrain rotation recrystallization and many relict grains exhibit core–mantle microstructures. Also, the relict grains are clearly more elongate than in samples farther away from the thrust.

Within the recess near Loch Srath nan Aisinnin, the footwall quartzites, in general, exhibit more highly strained microstructures than within the salient. Even the sample collected farthest from the Moine thrust at 141 m normal distance (nd) away, which is farther than any sample we examine from the salient, is partially recrystallized and exhibits core–mantle microstructures. When relict detrital grains are present, they are highly stretched and considerably undulose (Fig. 4b). The combination of recrystallization and stretched/flattened grains imparts a thrust-parallel mylonitic foliation to these rocks. This mylonitic foliation, along with the grains that define it, are occasionally kinked or otherwise folded. Rocks as far as 19 m nd from the thrust are completely recrystallized. These rocks display a prominent mylonitic banding, which is primarily defined by slight grain size variation from ≈10 to 25 μm and a minor amount of white mica. Adjacent to layers of relatively abundant mica are commonly mm- to cm-scale folds that verge in the transport direction. The recrystallized grains have a shape preferred orientation defining a foliation that is oblique to the mylonitic foliation by ≈40–50° and dips away from the transport direction (Fig. 4c).

The Moine schists composing the hanging wall rocks contain numerous microstructures that are consistent with WNW directed shearing. The mica-rich schist has ubiquitous folds that verge to the WNW, many of which are intrafolial folds. These fault rocks also exhibit a typical S-C fabric (Berthé et al., 1979) with a top-to-the-WNW sense of shear. The phyllosilicate layers occasionally contain transfer zones (i.e. microscopic flat–ramp–flats) and end in "horsetail splays," both of which are consistent with the known sense of shear (Fig. 4d). Quartz-rich layers within the schists exhibit similar microstructures to the recrystallized footwall quartzites. In particular, both the quartzites and the quartz-rich layers have a recrystallized grain-shape-fabric that is oblique to the mylonitic foliation. The Moine schist contains relatively harder opaque grains (mostly magnetite), which are loci for pressure shadow overgrowths. In the lineation-parallel, foliation-normal plane, the overgrowths are typically asymmetric with top-to-the-WNW sense of shear. In the foliation-parallel plane, the overgrowths form a radial pattern around the opaque grains suggesting non-plane-strain flattening deformation (Fig. 5). Away from the thrust surface, the mineralogic banding is less distinct and feldspar and biotite content increases but chlorite decreases. Moreover, grain size increases away from the thrust.

4.3. Quartz c-axis fabrics

The presence of subgrains, undulose extinction, etc. indicates that dislocation creep was important to the deformation. Therefore, a crystallographic preferred orientation should be expected. Indeed, within the entirely recrystallized samples, the grains flash nearly uniformly between blue and magenta when the gypsum plate is inserted and the microscope stage is rotated, indicating a strong crystallographic fabric.

The quartz *c*-axis fabric from the salient is separated into three groups: simple-shear dominated, pure-shear dominated, and random *c*-axis patterns (Fig. 6). The closest sample within the salient was collected at 1 m nd, at the Stack of Glencoul. At this distance from the thrust, the *c*-axis fabrics are already plane-strain and pure-shear dominated with symmetric Type I cross-girdles (Lister, 1977). Law et al. (1986) and Law (1987) demonstrated that closer to the thrust surface, at the Stack of Glencoul, asymmetric

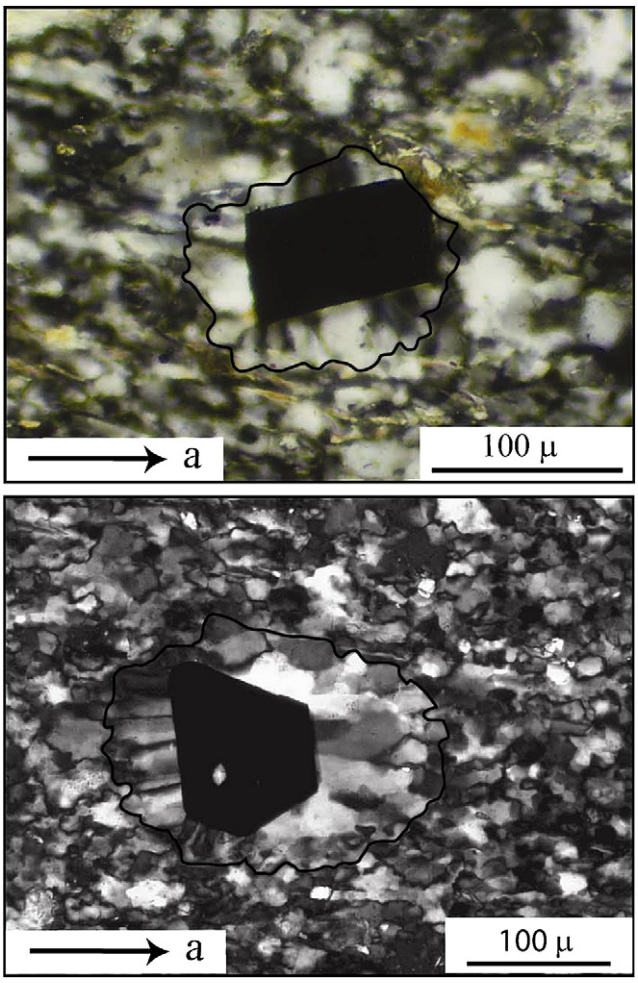

Fig. 5. Radial quartz overgrowths around opaque grains (probably magnetite) as viewed looking down on the foliation plane.

simple-shear dominated *c*-axis pattern transitions into a fully symmetric cross-girdle pattern by 30 cm nd (Fig. 6). Farther away from the thrust (at least ≈8 m nd), the *c*-axis patterns are diffuse with a relative lack of *c*-axes in the transport direction. By 43 m nd away from the thrust, the *c*-axis plots are random, indicating small crystal-plastic strain magnitudes (Fig. 6).

The quartz *c*-axis patterns from the recess can be grouped into two main categories: simple-shear dominated patterns and pure-shear dominated patterns. The simple-shear dominated patterns are asymmetric and indicate a top-to-the-WNW shearing direction. These asymmetric fabrics extend to at least 19 m nd beneath the thrust (Fig. 7). At Loch Srath nan Aisinnin, a gap in exposure from 19 to 42 m nd occurs. From 42 to 141 m nd, which is the closest quartzite outcrop to the Archean gneiss, the *c*-axis patterns are pure-shear dominated. In particular, the *c*-axis patterns approximate small-circle girdles, centered about the pole to the foliation, suggesting a non-plane-strain flattening deformation (i.e where $k \approx 0$). Some *c*-axis patterns appear to be a hybrid between a non-plane-strain flattening, small-circle girdle and a plane-strain flattening symmetric cross-girdle (Fig. 7). This hybrid suggests that the *k*-value is between 0 and 1. It is important to note that all samples from the recess have well defined *c*-axis fabrics.

The recess exhibits approximately small-circle girdle pure-shear dominated *c*-axis patterns whereas the salient has symmetric cross-girdle pure-shear dominated *c*-axis patterns. This contrast most likely represents a kinematic difference between the two

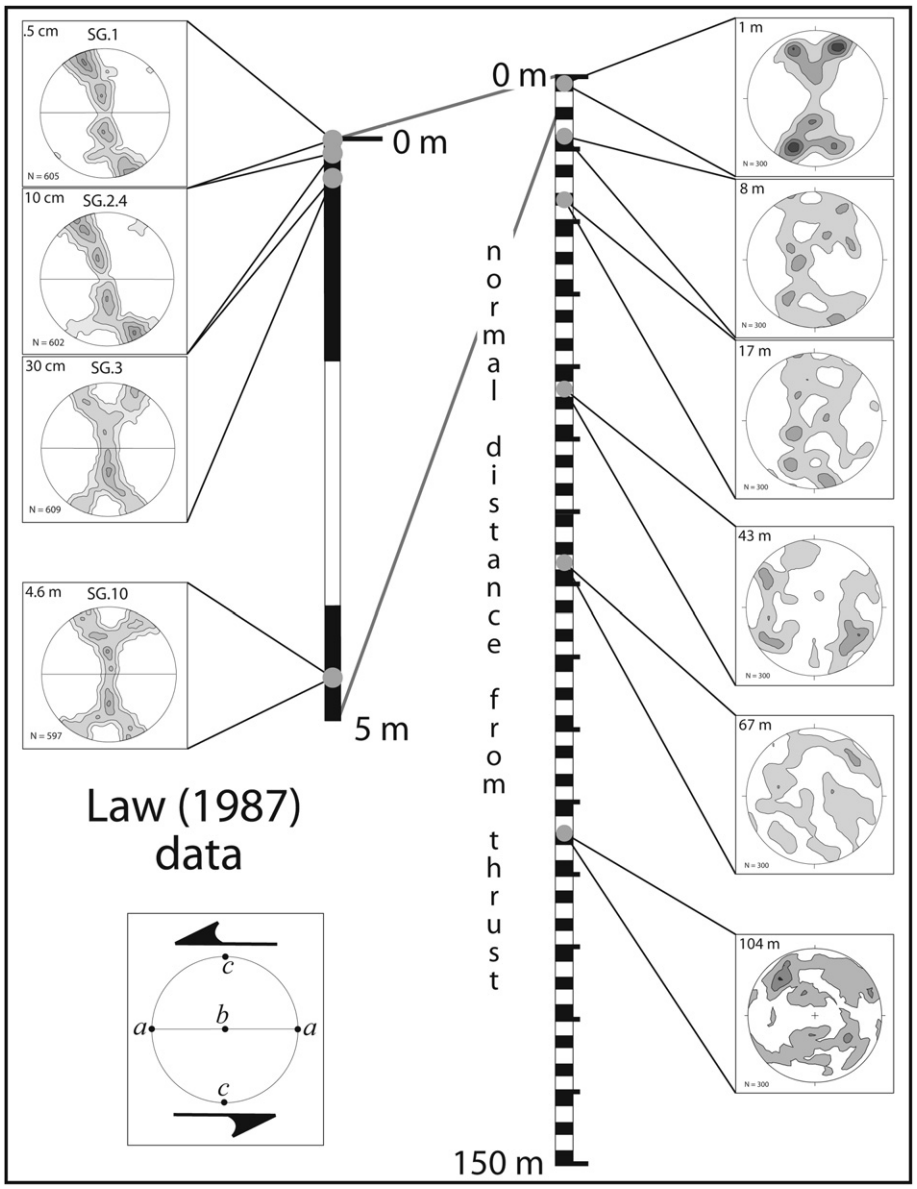

Fig. 6. Quartz *c*-axis textures from the salient plotted with respect to their normal distance below the thrust surface. To the left are data taken from Law (1987) collected at the Stack of Glencoul. Stereoplots are all equal-area lower hemisphere projections viewed toward the NNE. Foliation is vertical and oriented left–right and lineation is horizontal. Equal-area projection contour intervals are consecutive multiples of a uniform distribution.

areas, where the recess has greater non-plane-strain flattening deformation. Second, the asymmetric *c*-axis patterns persist nearly two orders of magnitude, in terms of distance from the fault, farther beneath the thrust surface within the recess than within the salient. Third, the *c*-axis fabrics persist farther beneath the thrust surface in the recess than within the salient, indicating that the recess is a larger as well as more intensely strained deformation zone.

4.4. Three-dimensional grain-shape approximations

We interpret the three-dimensional grain-shape data collected from relict grains to be a proxy for the finite strain tensor for a given sample. The recrystallized grains are more difficult to interpret. We suggest that the three-dimensional recrystallized grain shapes are a function of the strain state and therefore contain useful information about the kinematics of the deformation. Because recrystallizing grains attempt to achieve a steady-state shape and orientation, they cannot represent finite strain; however, they may represent incremental strain (Means, 1981; Ree, 1991). Also, a recrystallized grain boundaries should be able to move laterally with much more ease than a detrital grain-boundary because material does not need to flow, pushing adjacent material out of the way, for recrystallized grain boundaries to migrate. Low-temperature grain-boundary migration simply involves the reorganization of atoms into a differently oriented crystallographic lattice. Therefore, we think of recrystallized grains as representing incremental strain without the lateral boundary condition.

The relict grains have a relatively larger strain magnitude when compared with the recrystallized grains, as expected (Fig. 8). The recess has a relatively diverse population of ellipsoid shapes for the relict grains; however, it is interesting to note that all but one of the high-strained samples (i.e. $\varepsilon_S > 1$) have small *k*-values (i.e. less than 0.3), which is conservative allowing for volume loss during deformation. All but two samples from the salient plot within the general flattening field with a relatively even distribution of *k*-values between 1 and 0. The relict grains from the recess generally

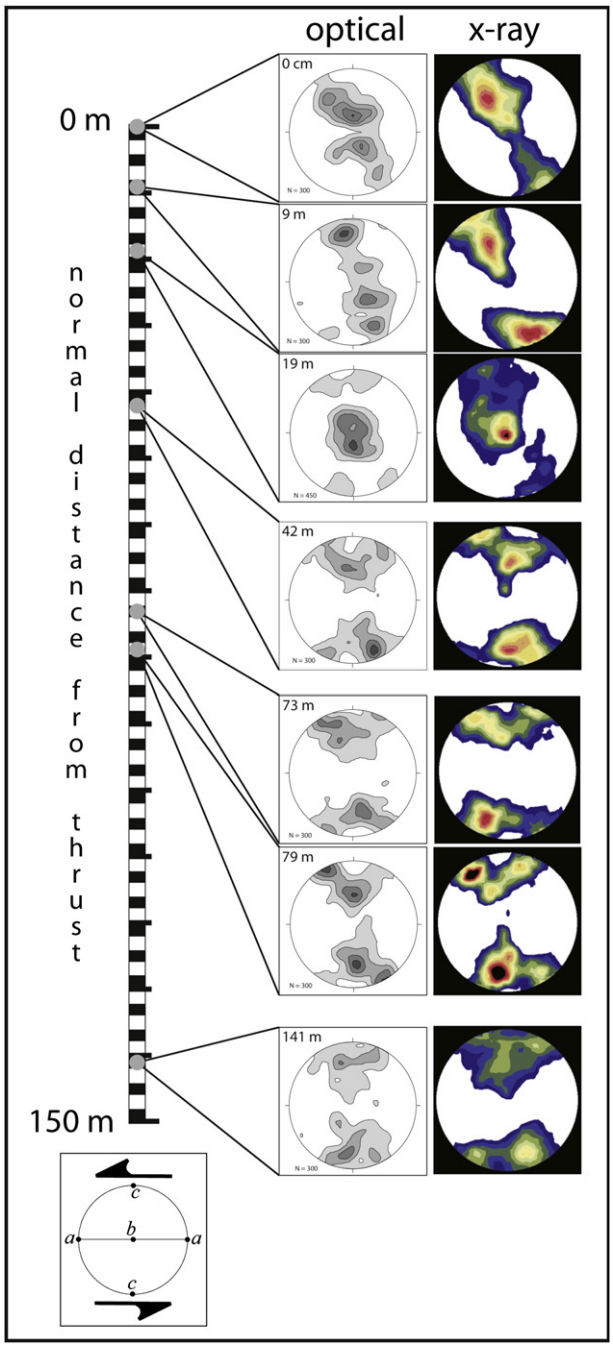

Fig. 7. X-ray and optically measured quartz *c*-axis textures from the recess plotted with respect to their normal distance below the thrust surface. Stereoplots are all equal-area lower hemisphere projections viewed toward the NNE. Foliation is vertical and oriented left–right and lineation is horizontal. Equal-area projection contour intervals are consecutive multiples of a uniform distribution.

record larger strain magnitudes (mean $\varepsilon_s = 0.89$) than the relict grains within the salient (mean $\varepsilon_s = 0.69$).

One limitation of the Flinn diagram is that the orientation of the strain ellipsoid is absent (Fig. 8). The fact that a strain ellipsoid lies on the plane-strain ($k = 1$) line on a Flinn plot is somewhat misleading if the ellipsoid's long and short axes are not approximately within the regional motion plane. In other words, a "plane strain" ellipsoid with its long axis oriented perpendicular to the transport direction would not represent a plane-strain deformation within the larger tectonic reference frame. Therefore, it is important to recognize strain ellipsoid orientations in conjunction with the Flinn diagram.

We observed that both the salient and the recess show evidence for a bimodal distribution in the orientations of the strain ellipsoid long axes. One maximum is sub-parallel to the regional transport direction and a smaller maximum is subperpendicular to the transport direction (Fig. 9). We consider this combination to be analogous to the lineation switching observed in transpressional zones (Tikoff and Greene, 1997). A thrust zone can be thought of as a transpressional zone "on its side" where the role of oblique convergence is taken up by gravity. The combination of gravitational flattening and tectonic contraction is constructive in the transport-perpendicular direction. Even though simple shear may be significant, coaxial pure shear is more efficient at accruing strain because each increment reinforces the previous increment, in contrast to the non-coaxial simple shear where the maximum extension direction is continually changing. The salient has more perpendicular grain lineations. 29% of the mean grain shapes are perpendicular to the transport direction in the salient, while only 13% of the mean grain shapes are perpendicular within the recess. We define a grain shape as being perpendicularly oriented if its trend is ±35° from the 202.5°–022.5° line (i.e. the line perpendicular to the regional transport direction).

5. Mathematical model

5.1. Model design

A more detailed model approach is found in Mookerjee and Mitra (2008), while here we describe key aspects needed for comparing model predictions to field data. We have constructed a numerical model of thrust wedge kinematics based on what we consider to be reasonable assumptions concerning five strain components for a deforming wedge: 1) thrust-parallel simple shear, 2) thrust-normal reaction strain, 3) horizontal contraction strain, 4) vertical gravitational strain, and 5) a lateral-confining boundary strain (Fig. 10). Points moving through the model wedge record detailed information about strain and particle paths. Moreover, incremental strains provide a virtual "snapshot" of the wedge kinematics.

We incorporated a flat–ramp–flat geometry into our model (Fig. 11) for comparison to the geometry near Loch Srath nan Aisinnin by using a simple wedge for the salient and a flat–ramp–flat for the recess (Figs. 11 and 12). Given that we assume that the wedges are the same length in the transport direction at both salient and recess, the recess wedge is thicker in the hinterland, which is consistent with critical taper theory (Chapple, 1978; Davis et al., 1983). For simplicity, we assume that the wedge has a steady-state topography such that erosion keeps pace with uplift (Willet, 1999). We recognize that steady states are ephemeral and that a deforming wedge lengthens and the taper angle decreases with time (Mitra, 1997; DeCelles and Mitra, 1995). However, these assumptions are first-order approximations that can represent a finite portion of the entire wedge deformation.

Next, we input our assumptions of how strain components vary throughout the wedge and within the underlying footwall. It has been a long-standing observation that shear strain increases dramatically toward the middle of natural shear zones (e.g. Ramsay and Graham, 1970; Mitra, 1979; Ramsay and Huber, 1983; Law, 1987). We describe this relationship with the equation: $\varepsilon_{ss} = e^{(\mathrm{Log}[\varepsilon_{ssmax}] + nd \cdot sf)}$, where ε_{ss} is the thrust-parallel simple shear, ε_{ssmax} is the amount of simple shear exactly at the thrust surface, nd is the normal distance away from the thrust, and sf is a shape factor that determines how rapidly the simple-shear strain tapers off away from the thrust surface (Fig. 13a). ε_{ssmax} and sf are input constants in our numerical model. We ran our model with ε_{ssmax} equal to $1\varepsilon_s$ and defined sf such that ε_{ss} equals 0.01 (octahedral shear strain, ε_s) at 1 km normal distance from the thrust.

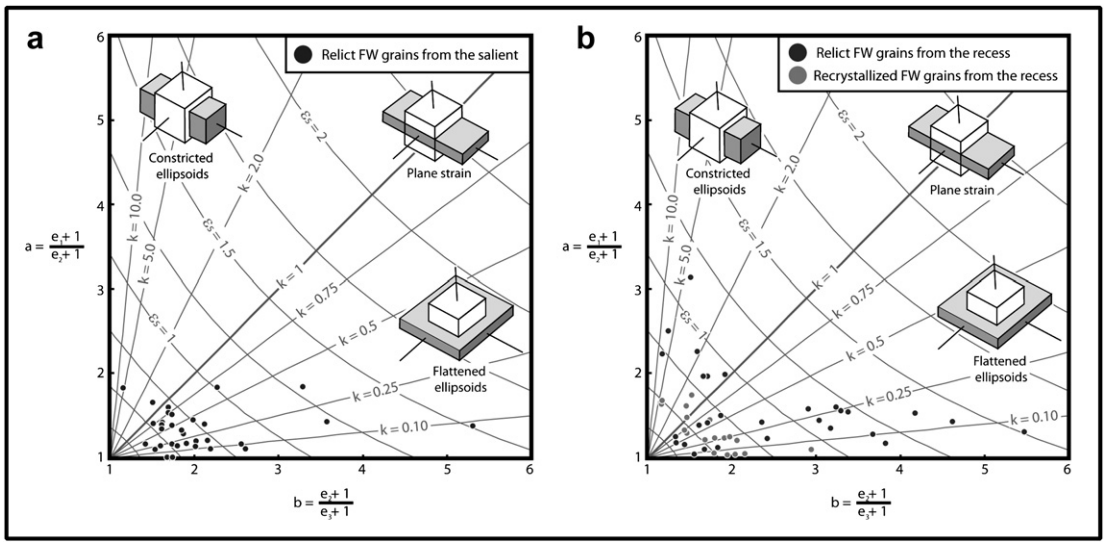

Fig. 8. Grain-shape data from the recess (a) and the salient (b) plotted on a Flinn diagram with calculated k and octahedral shear strain, ε_s, contours (Flinn, 1962). Both relict and recrystallized grain shapes are recorded for the recess.

We also assume that tectonic contraction, ε_{tc}, a horizontally oriented uniaxial shortening, decreases from the hinterland to the foreland (Fig. 13b). Many investigators have documented an increase in horizontal shortening toward the hinterland (e.g. Gwinn, 1970; Coward and Kim, 1981; Price, 1981; Mitra, 1994; Gray and Mitra, 1999). For a given segment of the fault, we impose an ε_{tc}; thus, ε_{tc} is proportional to the size of this segment (Fig. 13c). This proportionality, P, is dependent on the horizontal distance from the back of the wedge, d. We assume that $P(d)$ decreases linearly toward the fault tip where $P(d) = 0$. Once we have input the initial value for $P(0)$, this linear relationship is defined. Typically, we used 0.7 (ε_s) for this initial value. In addition to ε_{tc}, we also consider a thrust-normal reaction strain that is related to ε_{tc}. Given a dipping fault, not all tectonic contraction will shorten the rock horizontally because some strain will be "re-directed" such that a component of the shortening is directed normal to the fault (ε_{rxn}). ε_{rxn} is a uniaxial shortening strain oriented perpendicular to the thrust surface and is a direct result of Newton's third law of motion. Considering the tectonic contraction strain (ε_{tc}), the thrust-normal reaction strain (ε_{rxn}), and the dip of the fault (β), the greater the fault dip, the greater the reaction strain (Fig. 13c).

The effect of gravity on tectonic strains is not clear. Calculating the gravitational stresses for a given depth is a relatively trivial task if one assume that the overlying rocks have a constant density and Poisson's ratio (Means, 1976). However, determining the relationship between these stresses and their associated strains is anything but trivial. First, one must assume a constitutive relationship. Next, the constants for this relationship must be determined, but they depend on temperature, pressure and strain rate, which are likely to change as the material either strain-hardens or strain-softens (Griggs et al., 1960; Handin et al., 1963; Donath, 1970; Gleason and Tullis, 1995). In light of these uncertainties, we simply assume that the gravitational strain, ε_g, varies linearly with depth. Give that $\varepsilon_g = 0$ at the surface, we simply need to input the slope of this linear relationship. Acting conservatively, we define a slope that yields 0.08 (ε_s) at 15 km depth, ε_{g15k}. While the linear assumption is a simplification, we feel it is more accurate than either ignoring gravitational strain or assuming a constant flow law for the entire wedge. Increasing ε_{g15k} does not change the overall strain pattern for the wedge but does increase the amount of flattening.

The lateral-confining strain, ε_{BC}, is determined by establishing the maximum amount of lateral-confining strain for a given model run, ε_{bvmax}. At a given point, the incremental deformation matrix is calculated without a lateral boundary condition. Next, the lateral-confining strain needed for plane strain, ε_{bv}, is calculated. If ε_{bv} is less than ε_{bvmax}, then the confining strain, ε_{BC}, will be ε_{bv} and the deformation is plane strain. Conversely, if ε_{bv} is greater than ε_{bvmax},

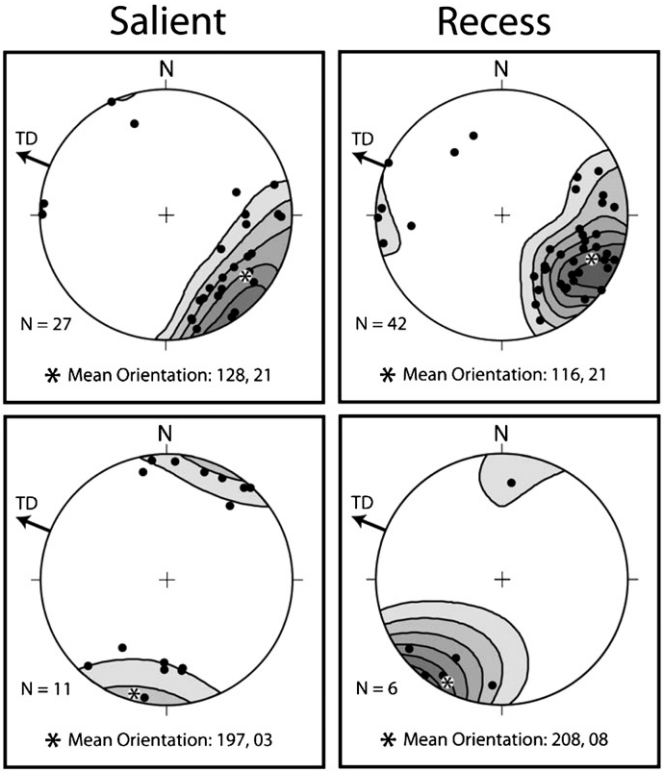

Fig. 9. The orientation of the grain-shape approximations plotted in the geographic reference frame for both the recess and the salient. The data has been divided into those that are sub-parallel to the transport direction and those that are perpendicular. The data is plotted on equal-area stereographic projections and contoured using Kamb's (1959) method with 1σ contour intervals. TD is the regional transport direction, 292.5 degrees.

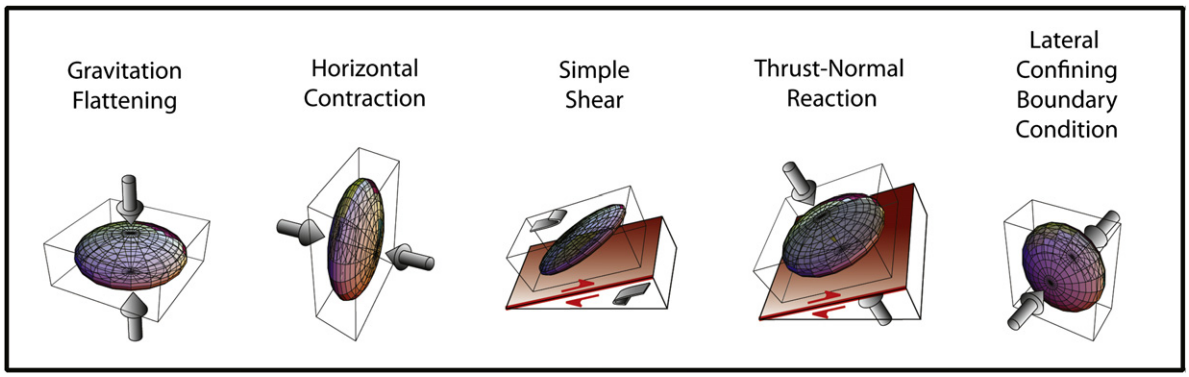

Fig. 10. The five strain components in our numerical model: gravitational strain (ε_g), horizontal contraction strain (ε_{tc}), simple-shear strain (ε_{ss}), thrust-normal reaction strain, (ε_{rxn}), and lateral-confining strain (ε_{bc}).

then ε_{BC} will equal ε_{bvmax} and the deformation is not plane strain (Fig. 14). Because we have no data or intuition for an appropriate value for ε_{bvmax}, we ran a series of models with incrementally increasing values of ε_{bvmax} ranging from 0 to 0.16.

A deformation matrix with all strain components is assembled. To avoid creating a sequencing of the five components, a velocity gradient matrix is first used to define the scenario:

$$L_g = \begin{bmatrix} \frac{\varepsilon_g}{\sqrt{6}} & 0 & 0 \\ 0 & \frac{\varepsilon_g}{\sqrt{6}} & 0 \\ 0 & 0 & \frac{2\cdot\varepsilon_g}{\sqrt{6}} \end{bmatrix} \tag{1}$$

$$L_{tc} = \begin{bmatrix} \frac{2\cdot\varepsilon_{tc}}{\sqrt{6}} & 0 & 0 \\ 0 & \frac{\varepsilon_{tc}}{\sqrt{6}} & 0 \\ 0 & 0 & \frac{\varepsilon_{tc}}{\sqrt{6}} \end{bmatrix} \tag{2}$$

$$L_{bv} = \begin{bmatrix} \frac{\varepsilon_{bv}}{\sqrt{6}} & 0 & 0 \\ 0 & \frac{2\cdot\varepsilon_{bv}}{\sqrt{6}} & 0 \\ 0 & 0 & \frac{\varepsilon_{bv}}{\sqrt{6}} \end{bmatrix} \tag{3}$$

$$L_{rxn} = \begin{bmatrix} \frac{\varepsilon_{rxn}}{\sqrt{6}} & 0 & 1 \\ 0 & \frac{\varepsilon_{rxn}}{\sqrt{6}} & 0 \\ 0 & 0 & \frac{2\cdot\varepsilon_{rxn}}{\sqrt{6}} \end{bmatrix} \tag{4}$$

$$L_{ss} = \begin{bmatrix} 1 & 0 & \gamma \\ 0 & 1 & 0 \\ 0 & 0 & 1 \end{bmatrix} \tag{5}$$

where γ is the shear strain calculated from ε_{ss} (see Appendix in Mookerjee and Mitra, 2008). Each velocity gradient matrices is constructed such that volume is conserved. Since L_g, L_{tc}, and L_{bv} are in different reference frames than L_{rxn} and L_{ss}, one of these sets of matrices needs to be rotated by the angle of the fault dip, φ, to be in the same reference frame as the others, so that the two sets can be added together. We have rotated L_{rxn} and L_{ss} such that they are within the "horizontal–vertical" reference frame. The sum of these five matrices yields:

$$L_{tot} = \begin{bmatrix} \frac{1}{6}\left(\sqrt{6}(\varepsilon_{bv}-2\varepsilon_{tc}+\varepsilon_g)+\sqrt{\frac{2}{3}}\cdot\varepsilon_{rxn}(-1+3Cos[2\phi])-3\cdot\gamma\cdot Sin[2\phi]\right) & 0 & \gamma\cdot Cos^2[\phi]+\sqrt{\frac{2}{3}}\cdot\varepsilon_{rxn}\cdot Cos[\phi]Sin[\phi] \\ 0 & \frac{-2\varepsilon_{bv}+\varepsilon_g+\varepsilon_{tc}+\varepsilon_{rxn}}{\sqrt{6}} & 0 \\ \frac{1}{2}\cdot Sin[\phi]\left(\sqrt{6}\cdot\varepsilon_{rxn}\cdot Cos[\phi]-2\cdot\gamma\cdot Sin[\phi]\right) & 0 & \frac{1}{6}\Big(-2\sqrt{6}\cdot\varepsilon_{rxn}\cdot Cos^2[\phi]+\sqrt{6}(\varepsilon_{bv}+\varepsilon_{tc}-2\varepsilon_g+\varepsilon_{rxn} \\ & & \cdot Sin^2[\phi]\Big)+3\cdot\gamma\cdot Sin[2\phi]\Big) \end{bmatrix} \tag{6}$$

Next, we calculate the deformation matrix using the differential equation: $L \bullet F = F'$ where L is the velocity gradient matrix, F is the deformation matrix and F' is the derivative of the deformation matrix (Bown, 1989). The resulting deformation matrix is:

$$F = \begin{pmatrix} \frac{1}{2}\Lambda\left(1+e^{\frac{\Omega}{\sqrt{2}}}-\frac{\left(-1+e^{\frac{\Omega}{\sqrt{2}}}\right)\left(\sqrt{3}\left(\varepsilon_{tc}-\varepsilon_g-\varepsilon_{rxn}\cdot Cos[2\phi]\right)+\sqrt{2}\cdot\gamma\cdot Sin[2\phi]\right)}{\Omega}\right) & 0 & \frac{\Lambda\left(-1+e^{\frac{\Omega}{\sqrt{2}}}\right)\cdot Cos[\phi]\cdot\left(\sqrt{2}\cdot\gamma\cdot Cos[\phi]+\sqrt{3}\cdot\varepsilon_{rxn}\cdot Sin[\phi]\right)}{\Omega} \\ 0 & e^{\frac{-2\varepsilon_{bv}+\varepsilon_{tc}+\varepsilon_g+\varepsilon_{rxn}}{\sqrt{6}}} & 0 \\ \frac{\Lambda\left(-1+e^{\frac{\Omega}{\sqrt{2}}}\right)Sin[\phi]\cdot\left(\sqrt{3}\varepsilon_{rxn}\cdot Cos[\phi]-\sqrt{2}\cdot\gamma\cdot Sin[\phi]\right)}{\Omega} & 0 & \frac{\Lambda\left(\left(1+e^{\frac{\Omega}{\sqrt{2}}}\right)\cdot\Omega+\left(-1+e^{\frac{\Omega}{\sqrt{2}}}\right)\left(\sqrt{3}\left(\varepsilon_{tc}-\varepsilon_g-\varepsilon_{rxn}\cdot Cos[2\phi]\right)+\sqrt{2}\cdot\gamma\cdot Sin[2\phi]\right)\right)}{2\Omega} \end{pmatrix} \tag{7}$$

where

$$\Omega = \sqrt{(3((\varepsilon_{tc}-\varepsilon_g)^2+\varepsilon_{rxn}^2)-2(\varepsilon_{tc}-\varepsilon_g)\cdot(3\cdot\varepsilon_{rxn}\cdot Cos[2\phi]-\sqrt{6}\cdot\gamma\cdot Sin[2\phi]))}$$

and $\Lambda = \mathbf{e}^{-\frac{\sqrt{3}\cdot(-2\varepsilon_{bv}+\varepsilon_{tc}+\varepsilon_g+\varepsilon_{rxn})+3\Omega}{6\sqrt{2}}}$. Ω and Λ have no physical meaning and are employed simply to conserve space. This deformation matrix is also constructed such that it preserves volume during deformation. The validity of this deformation matrix was tested by calculating highly precise approximations of simultaneous deformation via multiplying a series five million incremental deformation matrices.

Our numerical model of the hanging wall starts with a single line of observation points that is oriented perpendicular to the thrust surface (Fig. 12). These observation points are volumeless. With each deformation increment thrust-parallel displacement precedes a strain increment. At a given point, the values for each strain component are calculated and the deformation matrix assembled. While strain is assumed to be independent between points, displacement is dependent between points. In this way, successive displacement profiles are calculated for the entire wedge history. Furthermore, since each point at each increment has an associated deformation matrix, detailed strain histories can be calculated for each observation point and therefore the wedge as a whole.

The footwall portion of our numerical model is set up differently than the hanging wall. In the hanging wall, there is a single line of observation points that is translated along the thrust surface whereas in the in the footwall there are many lines of observations points that are not translated. The number of displacement profiles in the footwall equals the number of deformation increments in the hanging wall. To illustrate a kinematic history similar to the hanging wall, the deformation in the footwall is shown progressing from hinterland to foreland. In other words, the first displacement profile experiences $1/n_{inc}^{th}$ (where n_{inc} equals the number of increments for a given model run) of the finite deformation, the second displacement profile experiences $2/n_{inc}^{th}$, the third $3/n_{inc}^{th}$, and so on. This imposed illustration of kinematic history does not effect incremental calculations.

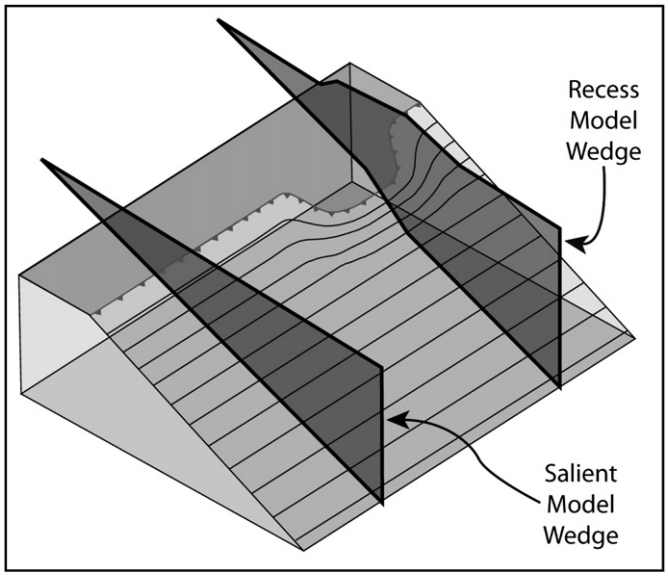

Fig. 11. A schematic illustration of the thrust surface geometry for a salient and recess pair along with the idealized cross-sectional geometry input into the numerical model for both the salient and the recess.

5.2. Model results

We color-coded observation points in model runs for the incremental strain magnitudes (octahedral shear strain), Flinn's *k*-parameter for the finite strain, and the lateral incremental strain (Fig. 15). Because of the computational cost, we generally limit our observations to the 5 km above and below the thrust surface. As expected, the incremental strain magnitudes are greatest closest to the thrust surface. The incremental strains are relatively elevated within the ramp segment of the model recess wedge and underlying footwall as compared to the flats. A subtle and unexpected pattern seen in the hanging wall of both the salient and recess incremental strain model wedges is the location of the areas of minimum strain. Moving upward from the thrust surface, the strain values reach a minimum value and then very gradually increase upward. This pattern is easiest to observe in the salient wedge where the incremental strain goes from light blue near the thrust to a dark blue and then back to a lighter blue approaching the top of the 5 km above the thrust surface. This strain pattern seems counterintuitive because we assumed upward decreasing strains (e.g. ε_g and ε_{ss}). Interestingly, it is this decrease in gravitational strain that causes an increase in total strain. If ε_{BC}, ε_g, and ε_{tc} were all equal in magnitude, strain would be absent because these strain components are mutually perpendicular. However, a decrease in one component results in an increase in strain, which is seen in our model thrust wedge as ε_g decreases upward. It would be unlikely to see this pattern in naturally deformed rocks because the strain variation is likely to be less than measurement error.

To further understand the effects that the ramp has on wedge kinematics, we examined spatial distribution of Flinn's *k*-value (Fig. 15b). Unlike the instantaneous strain, these values reflect the deformation history. In the hanging wall, once the observation points enter the ramp segment, their *k*-values decrease, giving rise to greater non-plane-strain flattening deformation. The hanging wall observation points, having traveled through the ramp segment, are transported into the upper flat where the *k*-values increase and the effect of the ramp begins to be overprinted. This distribution gives rise to *k*-value contours that we describe as having a 'kinked lozenge' shape. In the center of this lozenge, the *k*-values are greater than zero, but their long axes are perpendicular to the transport direction.

In addition to using Flinn's *k*-value to describe this non-plane-strain motion, we examine the incremental transport-perpendicular stretch (l/l_0). Because each deformed ellipsoid started as a unit sphere, the length of the perpendicular axis is equal to this length divided by the initial length and therefore is a measure of stretch. The maximum perpendicular stretch is within the ramp segment for the recess model wedge as one might expect

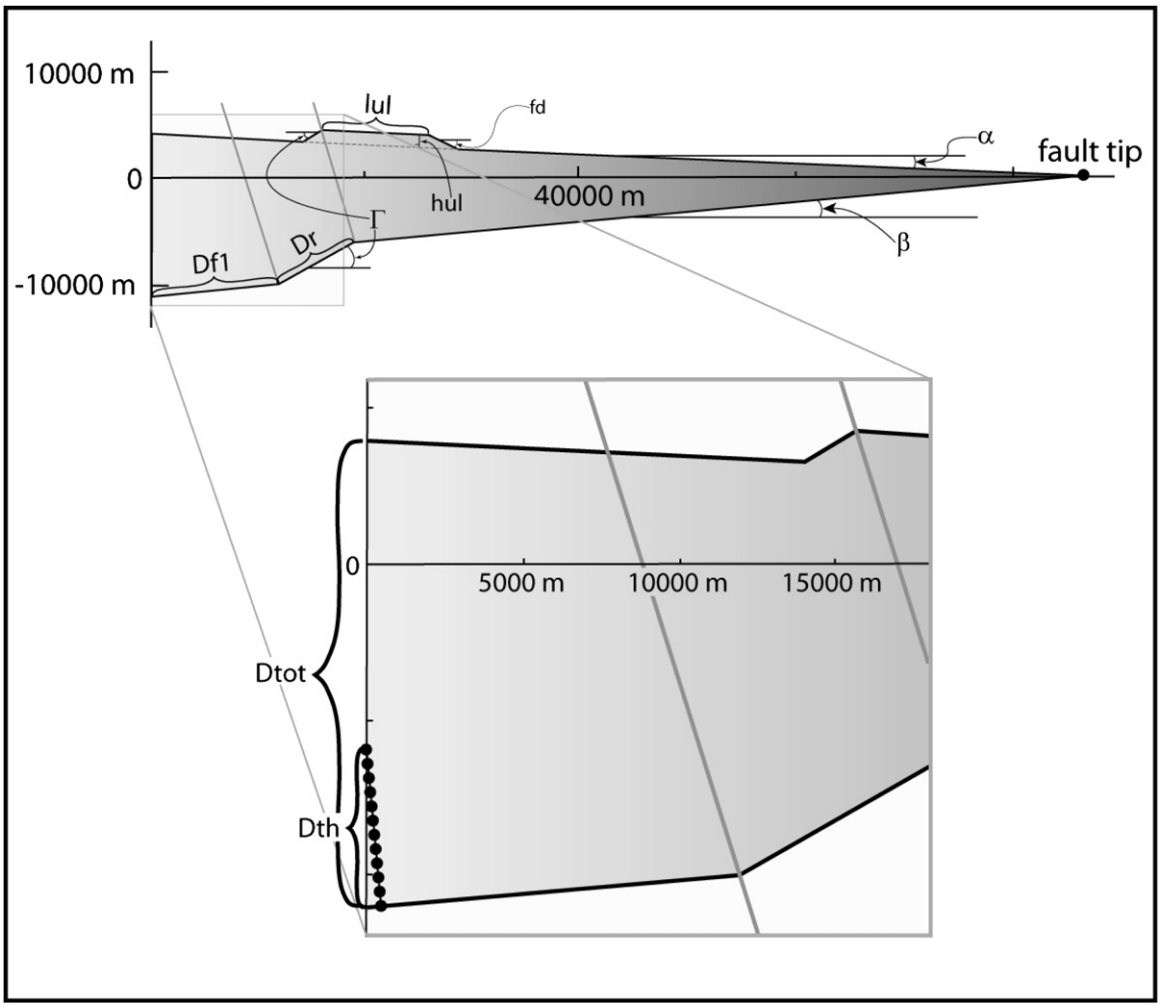

Fig. 12. The geometry of the deforming thrust wedge used in the numerical model and the initial position of the observation points within the hanging wall. Dtot, Df1, Dr, Dth, Γ, α, β, fd, lul, and hul are all input data. All other wedge parameters are calculated from these data.

considering the *k*-values demonstrating greater flattening within the ramp segment (Fig. 15c). However, the location of the maximum does not coincide with the center of our *k*-value kinked lozenge. In fact, it does not lie within the lozenge at all. In the hanging wall, the maximum stretch coincides with the area within the ramp segment that has the greatest depth and therefore largest ε_g. This area does not have the small *k*-values observed within the lozenge because it is so close to the thrust and therefore has a large component of simple shear. It may seem counterintuitive that the greatest out-of-the-plane motion is within an area of maximum plane-strain simple shear; however, simple shear does not hinder perpendicular flow and the relatively minor pure-shear components can efficiently accumulate significant lateral flow.

Finally, we ran a series of models to examine the effect of increasing the ε_{bvmax}. In particular, we wanted to observe how this parameter affected the orientation of the strain ellipsoid long axes, i.e. whether they are parallel or perpendicular to the transport direction. When $\varepsilon_{bvmax} = 0$ much of the wedge and underlying footwall have perpendicular lineations (Fig. 16d). Only where the deformation is dominated by simple shear, closest to the thrust, were lineations transport-parallel. As ε_{bvmax} increases (Fig. 16d–a), the domains with perpendicular lineations become smaller. The area most likely to develop perpendicular lineations is interestingly within the ramp segment (Fig. 16b). In fact, in the hanging wall, this area coincides with the *k*-value kinked lozenge. This relationship is because a strain ellipsoid that switches to having its long axis oriented perpendicular to the transport must first decrease its *k*-value to zero before starting to increase with its axis in the perpendicular direction. By continuing to increase ε_{bvmax}, the entire wedge will eventually have transport-parallel lineations (Fig. 16a) and undergo plane-strain deformation.

To gain an understanding of the magnitude of ε_{bvmax} for naturally deformed rocks, we determined the lateral-confining strain required to make the long axes parallel to the transport direction, $\varepsilon_{parallel}$, for each increment. Because the value of $\varepsilon_{parallel}$ is dependent on the number of increments, we compare this value to the strain magnitude of the deformation matrix prior to imposing a lateral boundary condition, $\varepsilon_{incwobc}$. During our model runs, we found that $\varepsilon_{parallel}$ could be as high as 42% of the deformation (i.e. $\varepsilon_{parallel}/(\varepsilon_{parallel} + \varepsilon_{incwobc})$). This result suggests that the lateral-confining strain may be the largest of the strain components if the maximum extension direction is parallel to the transport direction. We also found that ε_{bv} (the amount of lateral-confining strain necessary to have

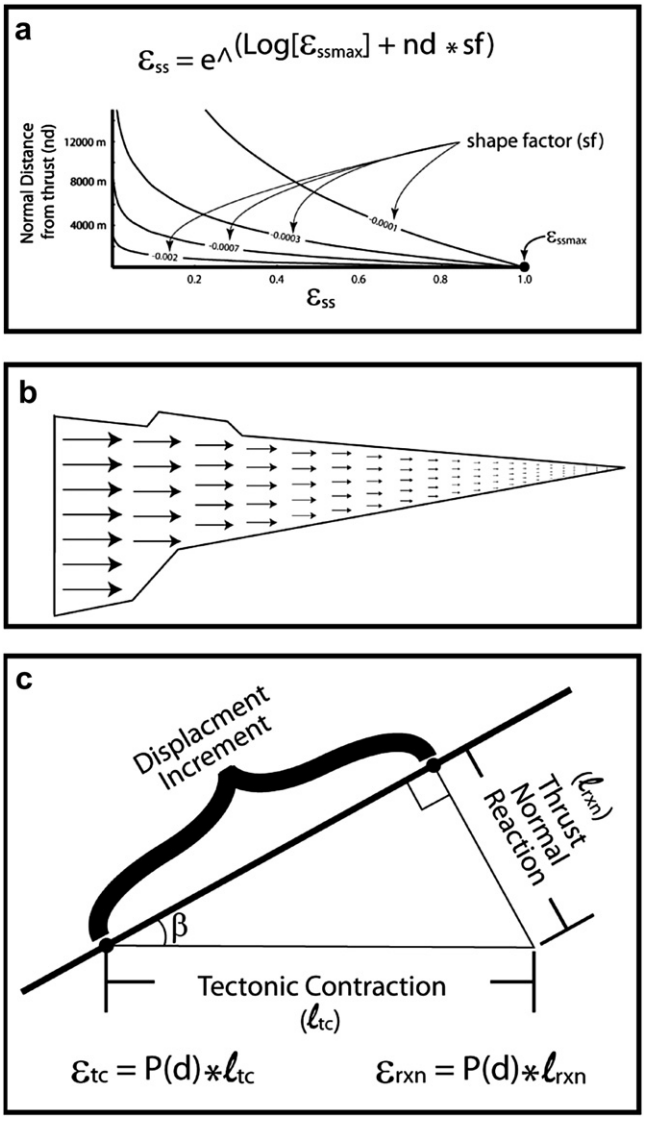

Fig. 13. Representation of how strain components vary within the model thrust wedge. a) The general form of the relationship between simple-shear strain, ε_{ss}, and the normal distance from the thrust surface, nd, assumed for the numerical model. ε_{ssmax} is the amount of simple shear exactly at the thrust surface, and the shape factor (sf) determines how quickly the simple-shear strain tapers off away from the thrust, b) a schematic diagram of how the tectonic contraction strain, ε_{tc}, varies throughout the wedge. This wedge has a vertical exaggeration of 2*x* the wedge used in the numerical model, c) the geometric relationship between the tectonic contraction length (l_{tc}), the thrust-normal reaction length (l_{rxn}), and the fault dip (β) for a given displacement increment. The horizontal contraction strain (ε_{tc}) and the thrust-normal reaction strain (ε_{rxn}) are dependent on these respective lengths.

a plane-strain deformation) could be as much as 46% of the deformation. We know that the ε_{BC} falls beneath this value for many naturally deformed rocks which record non-plane-strain deformation. Therefore, it should not be surprising that ε_{BC} can also be small enough in some environments to allow for transport-perpendicular lineations.

6. Discussion

Our kinematics-based model results exhibit significant similarities with the kinematic data obtained from the Moine thrust zone. First, the field data show that the strain magnitudes are greater within the recess than the adjoining salient. This relationship is evidenced by the three-dimensional grain-shape data as well as a greater degree of recrystallization. The mathematical model also shows increased strains in the vicinity of the ramp. Second, the field data demonstrates non-plane-strain flattening deformation within the recess. The Flinn's *k*-value from the high-strained relict grains, the small-circle girdle quartz *c*-axis fabrics and the radial quartz overgrowths within the foliation plane all suggest the deformation is dominated by non-plane-strain flattening. Our model, too, demonstrates minimum *k*-values within the ramp segment. Additionally, the ramp segment is the location of maximum transport-perpendicular stretch. Finally, both the salient and the recess yield evidence for transport-perpendicular maximum extension. Similarly, the numerical model shows evidence of transport-perpendicular maximum extension within both the salient and recess wedges. However, the model predicts that the ramp is where perpendicular lineation are most likely to form whereas the field data show that the salient has more transport-perpendicular grains than the recess. We suspect that this discrepancy arises from complexities within the three-dimensional strain field, which either resulted in a decrease in the lateral boundary conditions or an increase in one or more strain components yielding an element of lateral stretch within the salient.

In addition to varying ε_{bvmax}, it can be illustrative to vary other parameters that control the overall strain distribution. Varying these parameters can be thought of as changing the rheology of the deforming zone. For instance, the increase in either ε_{ssmax} or the shape factor (sf) results in an increase in *k*-values near the thrust surface (more closely plane strain, $k = 1$). Of course, strain magnitudes near the thrust increased. Further, by decreasing the slope of our linear ε_g vs. depth relationship, the model increases flattening strain and perpendicular stretch, and has a greater number of observation points with transport-perpendicular maximum extension directions within the deforming zone. Similarly, by increasing tectonic contraction (ε_{tc}), the amount of flattening, perpendicular stretch and transport-perpendicular extension increases. While changing these parameters alters the relative proportions of various strain components, the general pattern that the ramp is a regime of increased strain and greater out-of-plane motion is preserved.

Despite the above-mentioned discrepancy, the numerical model effectively recapitulates the field data, demonstrating the usefulness of this type of modeling. Therefore, kinematics-based modeling may yield insight into wedge kinematics that cannot be determined from the field data, such as strain path, or a more detailed picture of the finite and incremental strain patterns. The strain patterns observed in an upper flat segment of a thrust system might seem puzzling without considering the effect that traveling through a ramp segment can have on the finite strains. Subtle strain pattern may be beyond our ability to resolve given the errors associated with strain analysis. On the other hand, perhaps we simply have not thought to look for these patterns in the weakly strained rocks. In our view, numerical modeling is not about producing "concrete" or realistic numbers, but instead is more of a framework for helping an investigator better conceptualize an issue and steer her/his research focus. In particular, this model has drawn our attention to the need for a mechanism that redirects strain energy into the deforming hanging wall and footwall as a result of the increased difficulty in moving material up a ramped thrust surface.

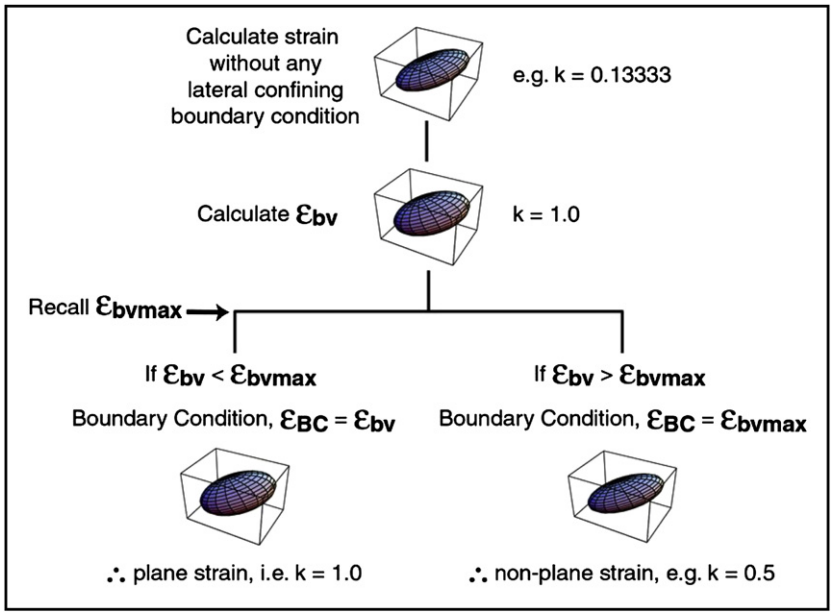

Fig. 14. A flow chart illustrating the process by which the numerical model determines the lateral-confining strain, ε_{BC}.

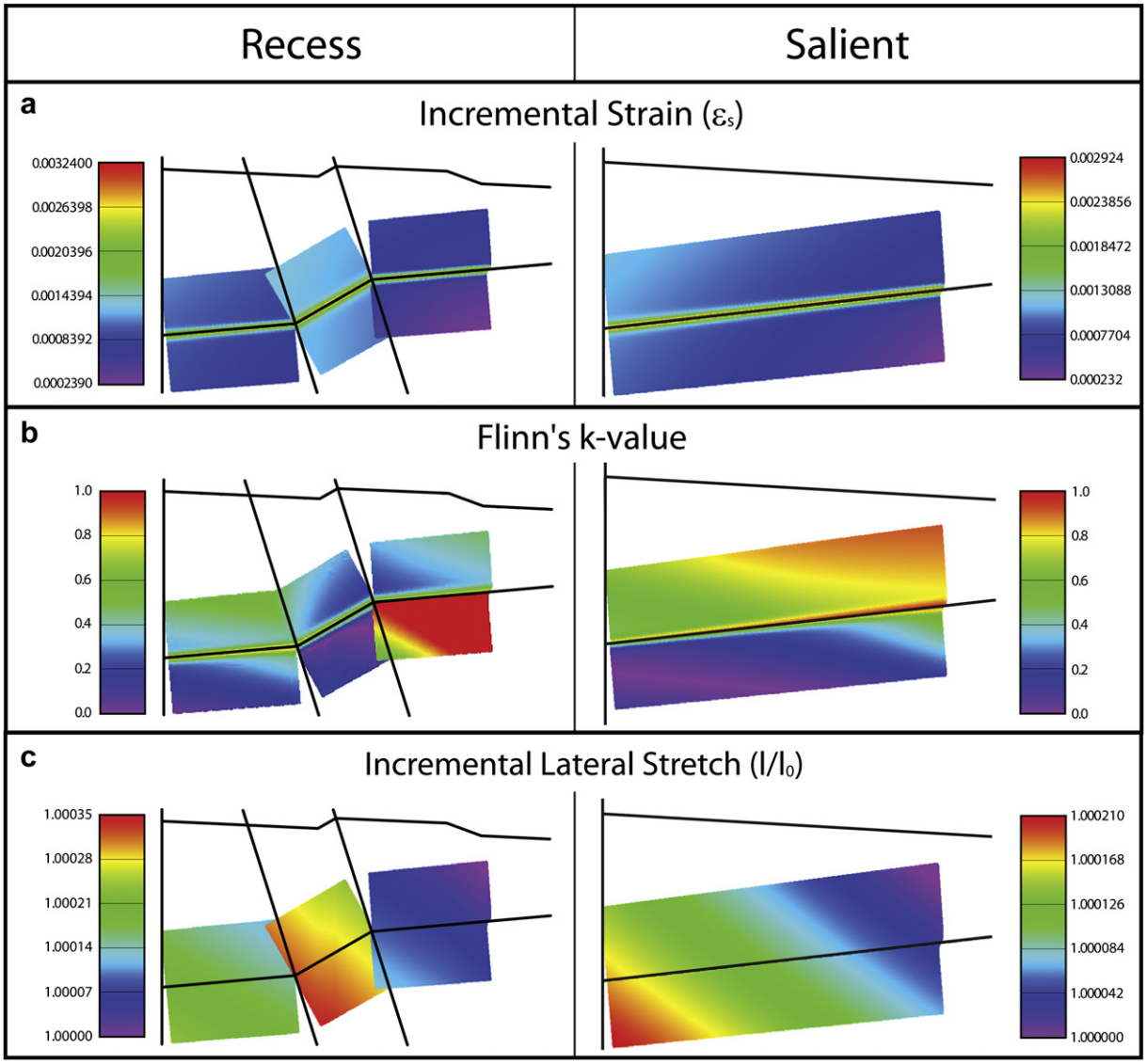

Fig. 15. Numerical model data for both the salient and recess model wedges. Each wedge includes a series of 300 displacement profiles. The wedges are color-coded to a) incremental octahedral shear strain, b) Flinn's *k*-value, and c) incremental lateral stretch. The adjacent scale bars illustrate our color spectrum with six specific values assigned to given hues.

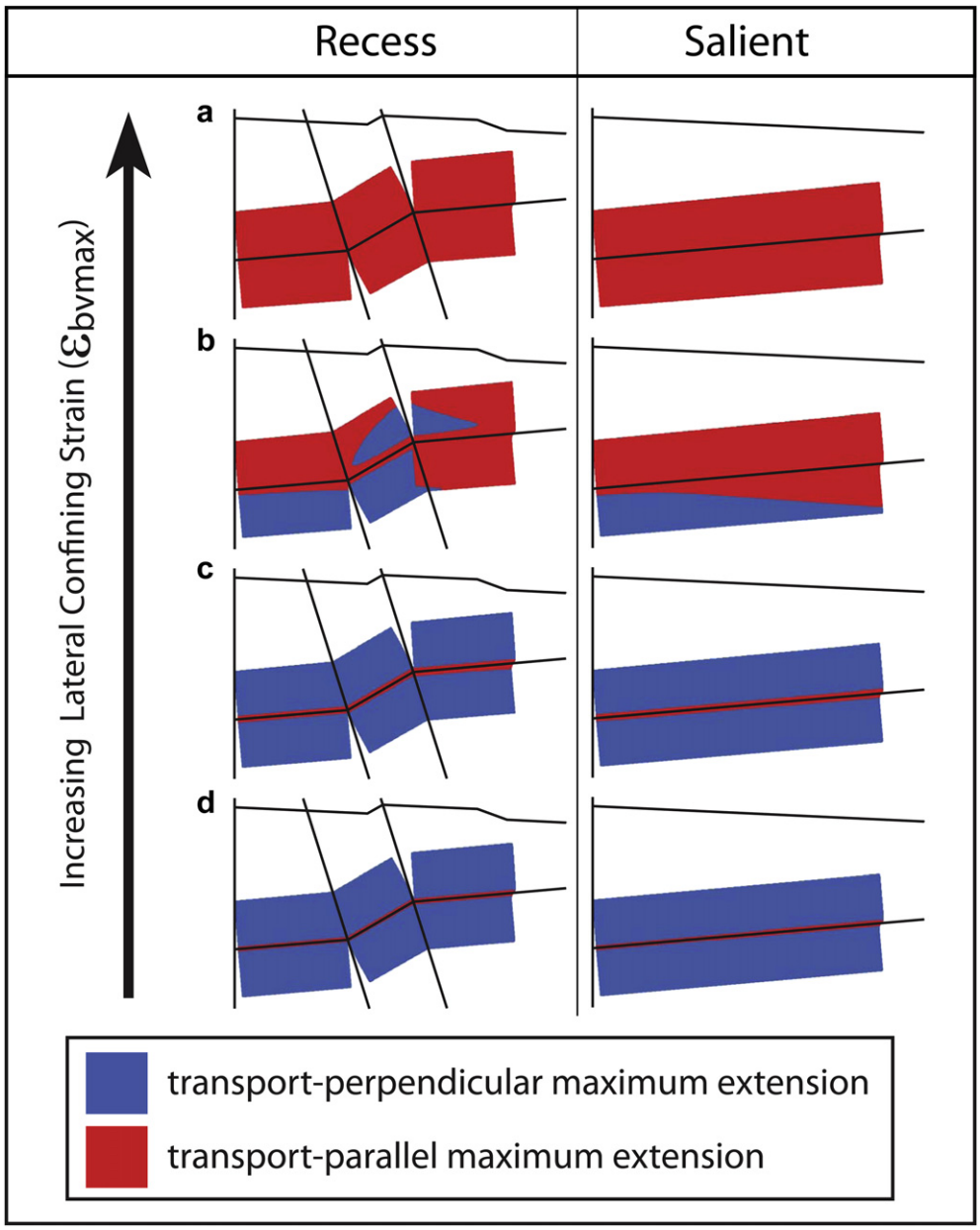

Fig. 16. A series of models runs for both the salient and recess model wedges where the maximum amount of lateral-confining strain, $\varepsilon_{bvmax,}$ is systematically varied. The red region represents observation points with finite strain ellipsoid long axes that lie within the motion plane. Blue regions represent finite strain ellipsoids with their long axes perpendicular to the motion plane. (a) $\varepsilon_{bvmax} = 0.160$, (b) $\varepsilon_{bvmax} = 0.095$, (c) $\varepsilon_{bvmax} = 0.0475$, (d) $\varepsilon_{bvmax} = 0.0$. Each wedge includes a series of 300 displacement profiles (for interpretation of the references to color in this figure legend, the reader is referred to the web version of this article).

7. Conclusions

The Moine thrust surface is non-planar and has been locally bowed up by the emplacement of a series of imbricate thrusts. This local fault steepening gives rise to a relative increase in stain magnitudes, microstructures, and flattening strains. Using a kinematics-based numerical model, we were able to generate similar results to our field observations, i.e. a corresponding increase in incremental octahedral shear strains, perpendicular stretch, and a decrease in Flinn's *k*-values associated with the ramp segment of our model wedge and underlying footwall. While these ramp segments can be relatively minor in areal extent, they may have a significant effect on the finite strains within the deformation zone and may have major implications for continued movement of the entire thrust system.

Acknowledgements

This work was supported by NSF grant EAR0208001 awarded to G. Mitra. This paper has benefited from useful conversations with Steven Wojtal and Sanghoon Kwon as well as constructive comments and criticisms of early drafts of this manuscript from Jay Paul Gates, and Shona Mookerjee. We would like to thank Carmie Garzione at the University of Rochester for the use of her microscope and printer. We would like to thank Holger Stunitz, at the University of Basel, for measuring *c*-axis textures via X-ray goniometry for eight quartzite samples. We also thank our reviewers, Ryan Thigpen, Dazhi Jiang and Scott Giorgis, and the editor Bill Dunne for their insightful comments and criticisms.

Appendix. Supplementary information

Supplementary information associated with this can be found at doi:10.1016/j.jsg.2009.08.012.

References

Alsop, G.I., Holdsworth, R.E., 1999. Vergence and facing patterns in large-scale sheath folds. Journal of Structural Geology 21, 1335–1349.

Alsop, G.I., Holdsworth, R.E., 2005. Discussion on "Evidence for non-plane strain flattening along the Moine thrust, Loch Srath nan Aisinnin, North-West Scotland" by Matthew Strine and Steven F. Wojtal. Journal of Structural Geology 27, 781–784.

Berthé, D., Choukroune, P., Jegouzo, P., 1979. Orthogneiss, mylonite, and non-coaxial deformation of granite: the example of the South Amorican shear zone. Journal of Structural Geology 1, 31–42.

Borradaile, G.J., 1984. Strain analysis of passive elliptical markers: success of de-straining methods. Journal of Structural Geology 6, 433–437.

Bown, R.M., 1989. Introduction to Continuum Mechanics for Engineers. Plenum Press, New York, p. 261.

Butler, R.W.H., 1984. Structural evolution of the Moine thrust belt between Loch More and Glen Dubh, Scotland. Scottish Journal of Geology 20, 161–179.

Carreras, J., Estrada, A., White, S.H., 1977. The effects of folding on the *c*-axis fabric of a quartz mylonite. Tectonophysics 39, 3–24.

Chapple, W.M., 1978. Mechanics of thin-skinned fold-and-thrust belts. Geological Society of America Bulletin 81, 1189–1198.

Christie, J.M., 1960. Mylonitic rocks from the Moine thrust zone between Loch Eriboll and Foinaven, NW Scotland. Transactions of the Edinburgh Geological Society 18, 79–93.

Christie, J.M., 1963. The Moine Thrust Zone in the Assynt Region, NW Scotland. In: University of California Publication of the Geological Society, vol. 40, pp. 345–419.

Cloos, H., 1946. Lineation: a critical review and annotated biography. Geological Society of America Memoir 18.

Cocks, L.R.M., Torsvik, T.H., 2006. European geography in a global context from the Vendian to the end of the Palaeozoic. In: European Lithosphere Dynamics. Geological Society, London, Memoirs 32, pp. 83–95.

Coward, M.P., 1988. The Moine thrust and the Scottish Caledonides. In: Mitra, G., Wojtal, S. (Eds.), Geometries and Mechanisms of Thrusting, with Special Reference to the Appalachians. Geological Society of America Special Paper 222, pp. 1–15.

Coward, M.P., Kim, J.H., 1981. Strain within thrust sheets. In: McClay, K.R., Price, N.J. (Eds.), Thrust and Nappe Tectonics. Geological Society of London Special Publication 9, pp. 275–292.

Coward, M.P., Nell, P.R., Talbot, J., 1992. An analysis of the strains associated with the Moine thrust zone, Assynt Northwest Scotland. In: Mitra, S., Fisher, G.W. (Eds.), Structural Geology of Fold and Thrust Belts, the Elliott Volume. Johns Hopkins University Press, pp. 105–122.

Dallmeyer, R.D., Strachan, R.A., Rogers, G., Watt, G.R., Friend, C.R.L., 2001. Dating deformation and cooling in the Caledonian thrust nappes of north Sutherland, Scotland; insights from $^{40}Ar/^{39}Ar$ and Rb–Sr chronology. Journal of the Geological Society of London 158, 501–512.

Davis, D., Suppe, J., Dahlen, F., 1983. Mechanics of fold-and-thrust belts and accretionary wedges. Journal of Geophysical Research B-88, 1153–1172.

DeCelles, P.G., Mitra, G., 1995. History of the Sevier orogenic wedge in terms of critical taper models, northeast Utah and southwest Wyoming. Geological Society of America Bulletin 107, 454–462.

Donath, R.A., 1970. Some information squeezed out of rocks. American Scientist 58, 54–72.

Durney, D.W., Ramsay, J.G., 1973. Incremental strains measured by syntectonic crystal growth. In: DeJong, K.A., Scholten, R. (Eds.), Gravity and Tectonics. John Wiley, New York, pp. 67–96.

Elliott, D., Johnson, M.R.W., 1980. Structural evolution in the northern part of the Moine thrust belt, NW Scotland. Transactions of the Royal Society of Edinburgh 71, 69–96.

Erickson, S.G., Jamison, W.R., 1995. Viscous–plastic finite-element models of fault-bend folds. Journal of Structural Geology 17, 561–573.

Evans, D.J., White, S.H., 1984. Microstructural and fabric studies from the rocks of the Moine Nappe, Eriboll, NW Scotland. Journal of Structural Geology 6, 369–389.

Flinn, D., 1962. On folding during three-dimensional progressive deformation. Quarterly Journal of the Geological Society of London 118, 385–433.

Freeman, S.R., Butler, R.W.H., Fliff, R.A., Rex, D.C., 1998. Direct dating of mylonite evolution: a multi-disciplinary geochronological study from the Moine thrust zone, NW Scotland. Journal of the Geological Society of London 155, 745–758.

Gilotti, J.A., Kumpulainen, R., 1986. Strain softening induced ductile flow in the Särv thrust sheet, Scandinadian Caledonides. Journal of Structural Geology 8, 441–455.

Gilotti, J.A., 1992. The rheologically critical matrix in arkosic mylonites along the Särv Thrust, Swedish Caledonides. In: Mitra, S., Fisher, G.W. (Eds.), Structural Geology of Fold and Thrust Belts, the Elliott Volume. Johns Hopkins University Press, pp. 145–160.

Gleason, G.C., Tullis, J., 1995. A flow law for dislocation creep of quartz aggregates determined with the molten salt cell. Tectonophysics 247, 1–23.

Gray, M.B., Mitra, G., 1999. Ramifications of four-dimensional progressive deformation in contractional mountain belts. Journal of Structural Geology 21, 1151–1160.

Griggs, D.T., Turner, F.J., Heard, H.G., 1960. Deformation of rocks at 500° to 800 °C. In: Griggs, D.T., Handin, J. (Eds.), Rock Deformation. Geological Society of America Memoir 79, pp. 39–104.

Gwinn, V., 1970. Kinematic Patterns and Estimates of Lateral Shortening, Valley and Ridge and Great Valley Provinces, Central Appalachians, South-Central Pennsylvania: Studies of Appalachian Geology, Central and Southern. Interscience Publication, New York, pp. 127–146.

Haneberg, W.C., 2004. Computational Geosciences with Mathematica. Springer-Verlag, Heidelberg, 381 pp.

Handin, J., Hager Jr., R.V., Friedman, M., Feather, J.N., 1963. Experimental deformation of sedimentary rocks under confining pressure: pore pressure tests. American Association of Petroleum Geologists Bulletin 47, 717–755.

Harris, A.L., Johnson, M.R.W., 1991. Moine. In: Craig, G.Y. (Ed.), Geology of Scotland, third ed.Geological Society of London, pp. 87–123.

Highton, A.J., Strachan, R.A., Holdsworth, R.E., Alsop, G.I., 2002. Loch Eriboll, Scotland Sheet 114W. Solid Geology 1:50000, Provisional Series. British Geological Survey.

Hirth, G., Tullis, J., 1992. Dislocation creep regimes in quartz aggregates. Journal of Structural Geology 14, 145–160.

Holdsworth, R.E., 1990. Progressive deformation structures associated with ductile thrusts in the Moine Nappe, Sutherland, N. Scotland. Journal of Structural Geology 12, 443–452.

Holdsworth, R.E., Alsop, G.I., Grant, C.J., Wilson, R.W., 2006. Thrust sequences and the significance of low-angle, out-of-sequence faults in the northernmost Moine Nappe and Moine thrust zone, NW Scotland. Journal of the Geological Society of London 163, 801–814.

Hossack, J.R., 1967. Pebble deformation and thrusting in the Bygdin Area (southern Norway). Tectonophysics 5, 315–339.

Johnson, M.R.W., 1983. Torridonian–Moine. In: Craig, G.Y. (Ed.), Geology of Scotland. Halsted Press, pp. 49–76.

Johnson, M.R.W., Kelley, S.P., Oliver, G.J.H., Winter, D.A., 1985. Thermal effects and timing of thrusting in the Moine thrust zone. Journal of the Geological Society of London 142, 863–874.

Kamb, W.B., 1959. Petrofabric observations from Blue Glacier, Washington. Journal of Geophysical Research 64, 1908–1909.

Kelley, S.P., 1988. The relationship between K–Ar mineral ages, mica grain sizes and movement on the Moine thrust zone, NW Highlands, Scotland. Journal of the Geological Society of London 145, 1–10.

Kelley, S.P., Powell, D., 1985. Relationships between marginal thrusting and movement on major, internal shear zones in the Northern Highland Caledonides, Scotland. Journal of Structural Geology 7, 161–174.

Kwon, S., Mitra, G., 2004. Strain distribution, stain history, and kinematic evolution associated with the formation of arcuate salients in fold–thrust belts: the example of the Provo salient, Sevier orogen, Utah. In: Sussman, A., Weil, A. (Eds.), Geological Society of America Special Paper 383, pp. 87–107.

Law, R.D., 1987. Heterogeneous deformation and quartz crystallographic fabric transitions: natural examples from the Moine thrust zone at the Stack of Glencoul, northern Assynt. Journal of Structural Geology 9, 819–834.

Law, R.D., Casey, M., Knipe, R.J., 1986. Kinematic and tectonic significance of microstructures and crystallographic fabrics within quartz mylonites from the Assynt and Eriboll regions of the Moine thrust zone, NW Scotland. Transactions of the Royal Society of Edinburgh, Earth Sciences 77, 99–126.

Lisle, R., 1985. Geological Strain Analysis; a Manual for the R_f/φ Technique. Pergamon Press, Oxford, 99 pp.

Means, W.D., 1976. Stress and Strain: Basic Concepts of Continuum Mechanics for Geologists. Springer-Verlag, New York, 339 pp.

Means, W.D., 1981. The concept of steady-state foliation. Tectonophysics 78, 179–199.

Mitra, G., 1979. Ductile deformation zones in the Blue Ridge basement rocks and estimation of finite strains. Geological Society of America Bulletin 90, 935–951.

Mitra, G., 1994. Strain variation in thrust sheets across the Sevier fold-and-thrust belt (Idaho–Utah–Wyoming): implications for section restoration and wedge taper evolution. Journal of Structural Geology 16, 585–602.

Mitra, G., 1997. Evolution of salients in a fold-and-thrust belt: the effects of sedimentary basin geometry, strain distribution and critical taper. In: Sengupta, S. (Ed.), Evolution of Geological Structures from Macro- to Micro-Scales. Chapman and Hall, London, pp. 59–90.

Mookerjee, M., Mitra, G., 2008. Kinematics-based mathematical model for deforming thrust wedges. Mathematical Geosciences 40, 249–275.

Mukul, M., Mitra, G., 1998. Finite strain and strain variation analysis in the Sheeprock thrust sheet: an internal thrust sheet in the Provo salient of the Sevier fold-and-thrust belt, Central Utah. Journal of Structural Geology 20, 403–417.

Nadai, A., 1963. Theory of Flow and Fracture of Solids. In: Engineering Societies Monographs. McGraw-Hill, New York, 705 pp.

Peach, B.N., Horne, J., Gunn, W., Clough, C.T., Hinxman, L.W., Teall, J.H.H., 1907. The geological structure of the northwest Highlands of Scotland. Memoir of the Geological Survey of Great Britain, 668 pp.

Price, R.A., 1981. The Cordilleran foreland thrust and fold belt in the southern Canadian Rocky Mountains. In: Price, N.J., McClay, K.R. (Eds.), Thrust and Nappe Tectonics. Geological Society of London Special Publication 9, pp. 427–428.

Ramsay, J.G., Graham, R.H., 1970. Strain variations in shear belts. Canadian Journal of Earth Sciences 7, 786–813.

Ramsay, J.G., Huber, M.I., 1983. The Techniques of Modern Structural Geology, vol. 1. Academic Press, London, 462 pp.

Ree, J.H., 1991. An experimental steady-state foliation. Journal of Structural Geology 13, 1001–1012.
Smart, K.J., Kreig, R.D., Dunne, W.D., 1999. Deformation behavior during blind thrust translation as a function of fault strength. Journal of Structural Geology 21, 855–874.
Strayer, L.M., Hudleston, P.J., 1997. Simultaneous folding and faulting and fold–thrust belt evolution: a distinct element model. Geological Society of America: Abstracts with Programs 29 (6), A44.
Strayer, L.M., Hudleston, P.J., 1998. Controls of duplex formation: results from numerical models. Geological Society of America: Abstracts with Programs 30 (7), A42.
Strine, M., Mitra, G., 2004. Preliminary kinematic data from a salient–recess pair along the Moine thrust, NW Scotland. In: Sussman, A., Weil, A. (Eds.), Geological Society of America Special Paper 383, pp. 87–107.
Strine, M., Wojtal, S.F., 2004. Evidence for non-plane strain flattening along the Moine thrust, Loch Srath nan Aisinnin, North-West Scotland. Journal of Structural Geology 26, 1755–1772.
Strine, M., Wojtal, S.F., 2005. Reply to the comments by Alsop and Holdsworth on "Evidence for non-plane strain flattening along the Moine thrust, Loch Srath nan Aisinnin, North-West Scotland" Journal of Structural Geology 27, 785–788.
Tikoff, B., Greene, D., 1997. Stretching lineations in transpressional shear zones. Journal of Structural Geology 19, 29–40.
Twiss, R.J., Unruh, J.R., 1998. Analysis of fault-slip inversions: do they constrain stress or strain rate. Journal of Geophysical Research 103, 12,205–12,222.
van Breemen, O., Aftalion, M., Johnson, M.R.W., 1979. Age of the Loch Borrolan complex, Assynt, and late movements along the Moine thrust zone. Journal of the Geological Society of London 136, 489–496.
Willet, 1992. Dynamic and kinematic growth and change of a Coulomb wedge. In: McClay, K.R. (Ed.), Thrust Tectonics. Chapman and Hall, London, pp. 19–31.
Willet, 1999. Orogeny and orography: the effects of erosion on the structure of mountain belts. Journal of Geophysical Research 104, 28,957–28981.
Wojtal, S.F., Mitra, G., 1986. Strain hardening and strain softening in fault zones from foreland thrusts. Geological Society of America Bulletin 97, 674–687.
Wojtal, S., Mitra, G., 1988. Nature of deformation in some fault rocks from Appalachian thrusts. In: Mitra, G., Wojtal, S. (Eds.), Geometries and Mechanisms of Thrusting, with Special Reference to the Appalachians. Geological Society of America Special Paper 222, pp. 17–33.